

# A node-based uniform strain virtual element method for elastoplastic solids

Rodrigo Silva-Valenzuela<sup>1,2</sup>, Alejandro Ortiz-Bernardin<sup>1\*</sup>,  
Edoardo Artioli<sup>3</sup>

<sup>1</sup>Computational and Applied Mechanics Laboratory, Department of Mechanical Engineering, Universidad de Chile, Av. Beauchef 851, Santiago, 8370456, Chile.

<sup>2</sup>Department of Mechanical Engineering, Universidad de La Serena, Av. Benavente 980, La Serena, 1720170, Chile.

<sup>3</sup>Dipartimento di Ingegneria “Enzo Ferrari”, Università degli Studi di Modena e Reggio Emilia, Via Pietro Vivarelli 10, Modena, 41125, Italy.

\*Corresponding author(s). E-mail(s): [aortizb@uchile.cl](mailto:aortizb@uchile.cl);  
Contributing authors: [rosilva@ug.uchile.cl](mailto:rosilva@ug.uchile.cl); [eartioli@unimore.it](mailto:eartioli@unimore.it);

## Abstract

A recently proposed node-based uniform strain virtual element method (NVEM) is here extended to small strain elastoplastic solids. In the proposed method, the strain is averaged at the nodes from the strain of surrounding linearly precise virtual elements using a generalization to virtual elements of the node-based uniform strain approach for finite elements. The averaged strain is then used to sample the weak form at the nodes of the mesh leading to a method in which all the field variables, including state and history-dependent variables, are related to the nodes and thus they are tracked only at these locations during the nonlinear computations. Through various elastoplastic benchmark problems, we demonstrate that the NVEM is locking-free while enabling linearly precise virtual elements to solve elastoplastic solids with accuracy.

**Keywords:** Virtual element method, Nodal integration, Strain averaging, Uniform strain, Volumetric locking, Elastoplasticity

# 1 Introduction

Elastoplastic solids demand advanced numerical techniques when using Galerkin-based approaches such as the finite element method (FEM) and the virtual element method (VEM). The need for advanced techniques has its roots in the presence of volumetric locking in the numerical solution due to the volume preserving nature of the plastic strain (plastic incompressibility condition) and in the volume preserving condition that arises when the Poisson's ratio approaches  $1/2$  (elastic incompressibility condition). Whichever is the source of the locking behavior, the standard lowest order elements in general perform poorly in problems that involve volume preserving conditions. In FEM, several approaches to deal with locking effects are found in the literature. An exhaustive review of these approaches is out of the scope of this paper, but we mention the most relevant ones: reduced/selective integration [1], B-bar technique [2, 3], mixed formulations [1], assumed strain methods [4], and nodal integration [5–14]. Of particular interest for the method proposed in this paper are nodal integration techniques. In these approaches, the Galerkin weak form is sampled at the nodes of the mesh leading to methods in which all the field variables (including state and history-dependent variables) are associated with the nodes.

The VEM is a generalization of the FEM to elements with arbitrary number of edges/faces (convex or nonconvex polytopes) known as virtual elements [15]. In its standard form, the method consists in the construction of an algebraic (exact) representation of the stiffness matrix without computation of basis functions (basis functions are *virtual*). In this process, a decomposition of the stiffness matrix into a consistency part and a stability part that ensures convergence of the method [16] is realized. The VEM has gained much interest in recent years and nowadays its applications can be found, for instance, in elastic and inelastic solids [17–25], elastodynamics [26, 27], finite deformations [28–36], contact mechanics [28, 37, 38], fracture mechanics [39–43], fluid mechanics [44–48], geomechanics [49, 50] and topology optimization [34, 51, 52].

In the VEM literature, there are few methods already developed that are suitable for modeling nearly incompressible elastic solids. These are generalizations of some of the above mentioned approaches for FEM. For instance, B-bar formulation [21, 26], mixed formulation [53], enhanced strain formulation [23], hybrid formulation [54], and nonconforming formulations [55–57]. In small strain elastoplasticity, the VEM literature is very limited. For instance, in Refs. [20, 58] high-order VEM has been used to improve the numerical performance when facing locking effects in elastoplastic solids. A mixed formulation based on a Hu-Washizu functional was adopted in Ref. [25]. Recently, a stabilization-free hybrid virtual element method has been proposed for elastoplastic solids that is locking-free [59].

In this paper, the recently proposed node-based uniform strain virtual element method [60] (NVEM) is extended to small strain elastoplastic solids. In the proposed approach, the strain is averaged at the nodes from the strain of surrounding linearly precise virtual elements using a generalization to virtual elements of the node-based uniform strain approach for finite elements [6]. The nodal strain that results from the averaging process is interpreted as the nodal sample of the strain in the nodal integration of the weak form. Consequently, the nodal strain is also used at the constitutive

evaluation level. As in any nodal integration method, the state and history-dependent variables in the NVEM become associated with the nodes. In practice, this means that in nonlinear computations these variables are tracked only at the nodes. This feature can be exploited to avoid mesh remapping of these variables in Lagrangian large deformation simulations with remeshing (see, for instance, Ref. [9]), which is not possible when Gauss integration is used. We do not intend to explore the latter feature in this paper as the focus here is on the small strain regime, which is a necessary intermediate step towards developments in the finite strain regime.

The remainder of this paper is structured as follows. In Section 2, the NVEM for small strain elastoplasticity is developed. The elastoplastic constitutive model used and the stabilization proposed for the NVEM are presented in Section 3. In Section 4, various elastoplastic benchmark problems are considered to assess the performance of the NVEM. The paper ends with a summary and conclusions in Section 5.

## 2 Node-based uniform strain virtual element method

In this section, the basics of the node-based uniform strain virtual element method (NVEM), which was developed in Ref. [60], is summarized. The method belongs to the Galerkin weak formulation family of methods. In this sense, we consider an elastic body that occupies the open domain  $\Omega \subset \mathbb{R}^2$  and is bounded by the one-dimensional surface  $\Gamma$  whose unit outward normal is  $\mathbf{n}_\Gamma$ . The boundary is assumed to admit decompositions  $\Gamma = \Gamma_D \cup \Gamma_N$  and  $\emptyset = \Gamma_D \cap \Gamma_N$ , where  $\Gamma_D$  is the Dirichlet boundary and  $\Gamma_N$  is the Neumann boundary. The closure of the domain is  $\overline{\Omega} = \Omega \cup \Gamma$ . Let  $\mathbf{u}(\mathbf{x}) : \overline{\Omega} \rightarrow \mathbb{R}^2$  be the displacement field at a point of the elastic body with position vector  $\mathbf{x}$  when the body is subjected to external tractions  $\mathbf{t}_N(\mathbf{x}) : \Gamma_N \rightarrow \mathbb{R}^2$  and body forces  $\mathbf{b}(\mathbf{x}) : \Omega \rightarrow \mathbb{R}^2$ . The imposed Dirichlet (essential) boundary conditions are  $\mathbf{u}_D(\mathbf{x}) : \Gamma_D \rightarrow \mathbb{R}^2$ . The displacement field  $\mathbf{u}(\mathbf{x}) \in \mathcal{V}$  is found such that (weak form)

$$a(\mathbf{u}, \mathbf{v}) = \ell(\mathbf{v}) \quad \forall \mathbf{v}(\mathbf{x}) \in \mathcal{W},$$

$$a(\mathbf{u}, \mathbf{v}) = \int_{\Omega} \boldsymbol{\sigma}(\mathbf{u}) : \boldsymbol{\varepsilon}(\mathbf{v}) \, d\mathbf{x}, \quad \ell(\mathbf{v}) = \int_{\Omega} \mathbf{b} \cdot \mathbf{v} \, d\mathbf{x} + \int_{\Gamma_N} \mathbf{t}_N \cdot \mathbf{v} \, ds, \quad (1)$$

where  $\mathcal{V}$  denotes the space of admissible displacements and  $\mathcal{W}$  the space of its variations;  $\boldsymbol{\sigma}$  is the Cauchy stress tensor and  $\boldsymbol{\varepsilon}$  is the small strain tensor that is given by

$$\boldsymbol{\varepsilon}(\mathbf{u}) = \frac{1}{2} (\mathbf{u} \otimes \nabla + \nabla \otimes \mathbf{u}). \quad (2)$$

### 2.1 Virtual element method

The weak form (1) is the continuous problem. The discrete problem is formulated on a partition of the domain  $\Omega$  into nonoverlapping elements with arbitrary number of edges (convex or non-convex polygons). This partition is denoted by  $\mathcal{T}_h$ , where  $h$  is the maximum diameter of any element in the partition. An element in the partition is denoted by  $E$  and its boundary by  $\partial E$ .  $|E|$  is the area of the element and  $N_E^V$  its number of edges/nodes. The unit outward normal to the element boundary in the

Cartesian coordinate system is denoted by  $\mathbf{n} = [n_1 \ n_2]^\top$ . Fig. 1 depicts an element with seven edges ( $N_E^V = 7$ ), where the edge  $e_a$  of length  $|e_a|$  and the edge  $e_{a-1}$  of length  $|e_{a-1}|$  are the element edges incident to node  $a$ , and  $\mathbf{n}_a$  and  $\mathbf{n}_{a-1}$  are the unit outward normals to these edges, respectively.

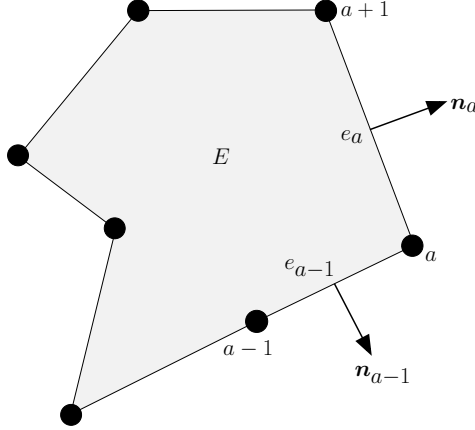


**Fig. 1:** Schematic representation of a polygonal element of  $N_E^V = 7$  edges

Following a standard Galerkin approach, we assume approximations of  $\mathbf{u}$  and  $\mathbf{v}$  on the element, as follows:

$$\begin{aligned} \mathbf{u}_h &= \begin{Bmatrix} u_{1h} \\ u_{2h} \end{Bmatrix} = \sum_{a=1}^{N_E^V} \phi_a(\mathbf{x}) \mathbf{u}_a, & \mathbf{u}_a &= \begin{Bmatrix} u_{1a} \\ u_{2a} \end{Bmatrix}, \\ \mathbf{v}_h &= \begin{Bmatrix} v_{1h} \\ v_{2h} \end{Bmatrix} = \sum_{a=1}^{N_E^V} \phi_a(\mathbf{x}) \mathbf{v}_a, & \mathbf{v}_a &= \begin{Bmatrix} v_{1a} \\ v_{2a} \end{Bmatrix}. \end{aligned} \quad (3)$$

where  $\{\phi_a(\mathbf{x})\}_{a=1}^{N_E^V}$  are basis functions that form a partition of unity. A peculiarity of the VEM is that the basis functions are never computed, which is why they are considered *virtual*. For the method to work, we only need to assume their behavior on the element boundary. For linearly precise VEM approximations, the basis functions on the element boundary are assumed to be

- piecewise linear (edge by edge),
- continuous on the element edges,

which means that the basis functions possess the Kronecker-delta property on the element edges, and hence they behave like the one-dimensional hat function.

At the element level, the following discrete local spaces are defined:

$$\mathcal{V}_h|_E := \{\mathbf{u}_h(\mathbf{x}) : \mathbf{u}_h \in \mathcal{V}(E)\}, \quad \mathcal{W}_h|_E := \mathcal{V}_h|_E.$$

The discrete local spaces are assembled to form the following discrete global spaces:

$$\begin{aligned} \mathcal{V}_h &:= \{\mathbf{u}(\mathbf{x}) \in \mathcal{V} : \mathbf{u}|_E \in \mathcal{V}_h|_E \quad \forall E \in \mathcal{T}_h\}, \\ \mathcal{W}_h &:= \{\mathbf{v}(\mathbf{x}) \in \mathcal{W} : \mathbf{v}|_E \in \mathcal{V}_h|_E \quad \forall E \in \mathcal{T}_h\}. \end{aligned}$$

Using the preceding definitions, the discrete version of the weak form (1) reads: find  $\mathbf{u}_h \in \mathcal{V}_h$  such that

$$\sum_{E \in \mathcal{T}_h} a_E(\mathbf{u}_h, \mathbf{v}_h) = \sum_{E \in \mathcal{T}_h} \ell_E(\mathbf{v}_h) \quad \forall \mathbf{v}_h \in \mathcal{W}_h. \quad (4)$$

To obtain the discrete weak form for the VEM, we follow the standard VEM literature (see for instance, Ref. [61]). We first define a projection operator  $\Pi$  onto the space of polynomials of degree 1. To this end, let  $[\mathcal{P}(E)]^2$  represent the space of polynomials of degree 1 over the element  $E$ . The projection operator  $\Pi$  is defined as:

$$\Pi : \mathcal{V}_h|_E \rightarrow [\mathcal{P}(E)]^2, \quad \Pi \mathbf{p} = \mathbf{p} \quad \forall \mathbf{p} \in [\mathcal{P}(E)]^2. \quad (5)$$

$\Pi$  is then used to split the displacement approximation on the element, as follows:

$$\mathbf{u}_h = \Pi \mathbf{u}_h + (\mathbf{u}_h - \Pi \mathbf{u}_h), \quad (6)$$

where  $\Pi \mathbf{u}_h$  is the polynomial part of  $\mathbf{u}_h$  (of degree 1) and  $\mathbf{u}_h - \Pi \mathbf{u}_h$  contains its remainder terms. The remainder terms can contain polynomials of order greater than 1 or even nonpolynomial terms. The actual form of the projection  $\Pi \mathbf{u}_h$  is obtained from the orthogonality condition:  $\forall \mathbf{p} \in [\mathcal{P}(E)]^2$ ,

$$a_E(\mathbf{u}_h - \Pi \mathbf{u}_h, \mathbf{p}) = a_E(\mathbf{p}, \mathbf{v}_h - \Pi \mathbf{v}_h) = 0, \quad (7)$$

which, at the element level, gives [22, 62–64]

$$\Pi \mathbf{u}_h = \begin{bmatrix} (x_1 - \bar{x}_1) & 0 & \frac{(x_2 - \bar{x}_2)}{2} & 1 & 0 & \frac{(x_2 - \bar{x}_2)}{2} \\ 0 & (x_2 - \bar{x}_2) & \frac{(x_1 - \bar{x}_1)}{2} & 0 & 1 & \frac{(x_1 - \bar{x}_1)}{2} \end{bmatrix} \begin{Bmatrix} \hat{\varepsilon}_{11} \\ \hat{\varepsilon}_{22} \\ 2\hat{\varepsilon}_{12} \\ \bar{u}_1 \\ \bar{u}_2 \\ 2\hat{\omega}_{12} \end{Bmatrix}, \quad (8)$$

where  $\bar{x}_1$  and  $\bar{x}_2$  are the components of the mean of the values that the position vector  $\mathbf{x} = [x_1 \ x_2]^\top$  takes over the vertices of the element; i.e.,

$$\bar{\mathbf{x}} = \begin{Bmatrix} \bar{x}_1 \\ \bar{x}_2 \end{Bmatrix} = \frac{1}{N_E^V} \sum_{a=1}^{N_E^V} \mathbf{x}(\mathbf{x}_a), \quad (9)$$

where  $\mathbf{x}_a = [x_{1a} \ x_{2a}]^\top$  are the coordinates of node  $a$ ;  $\bar{u}_1$  and  $\bar{u}_2$  are the components of the mean of the values that the displacement approximation  $\mathbf{u}_h = [u_{1h} \ u_{2h}]^\top$  takes over the vertices of the element; i.e.,

$$\bar{\mathbf{u}} = \begin{Bmatrix} \bar{u}_1 \\ \bar{u}_2 \end{Bmatrix} = \frac{1}{N_E^V} \sum_{a=1}^{N_E^V} \mathbf{u}_h(\mathbf{x}_a), \quad (10)$$

In other words,  $\bar{\mathbf{x}}$  and  $\bar{\mathbf{u}}$  represent the geometric center of the element and its associated displacement vector, respectively; the terms  $\hat{\varepsilon}_{ij}$  are components of the element average

$$\hat{\varepsilon}(\mathbf{u}_h) = \frac{1}{|E|} \int_E \boldsymbol{\varepsilon}(\mathbf{u}_h) d\mathbf{x} = \frac{1}{2|E|} \int_{\partial E} (\mathbf{u}_h \otimes \mathbf{n} + \mathbf{n} \otimes \mathbf{u}_h) ds, \quad (11)$$

and  $\hat{\omega}_{12}$  is the component of the element average

$$\hat{\omega}(\mathbf{u}_h) = \frac{1}{|E|} \int_E \boldsymbol{\omega}(\mathbf{u}_h) d\mathbf{x} = \frac{1}{2|E|} \int_{\partial E} (\mathbf{u}_h \otimes \mathbf{n} - \mathbf{n} \otimes \mathbf{u}_h) ds, \quad (12)$$

where  $\boldsymbol{\omega}(\mathbf{u}_h)$  is the skew-symmetric tensor that represents rotations.

On substituting (6) into (4), and using the orthogonality condition (7) and noting that  $\mathbf{u}_h$  and  $\mathbf{v}_h \in [\mathcal{P}(E)]^2$ , leads to the following VEM representation of the discrete weak form: find  $\mathbf{u}_h \in \mathcal{V}_h$  such that

$$\sum_{E \in \mathcal{T}_h} \left[ a_E(\Pi \mathbf{u}_h, \Pi \mathbf{v}_h) + s_E(\mathbf{u}_h - \Pi \mathbf{u}_h, \mathbf{v}_h - \Pi \mathbf{v}_h) \right] = \sum_{E \in \mathcal{T}_h} \ell_E(\Pi \mathbf{v}_h) \quad \forall \mathbf{v}_h \in \mathcal{V}_h, \quad (13)$$

where  $s_E(\mathbf{u}_h - \Pi \mathbf{u}_h, \mathbf{v}_h - \Pi \mathbf{v}_h)$  is a computable approximation to  $a_E(\mathbf{u}_h - \Pi \mathbf{u}_h, \mathbf{v}_h - \Pi \mathbf{v}_h)$  and is meant to provide stability.

## 2.2 Nodal averaging operator

The VEM as described above is prone to volumetric locking in the limit  $\nu \rightarrow 1/2$ . Using the virtual element mesh and considering a typical nodal vertex  $I$ , the NVEM that was proposed in Ref. [60] applies a nodal averaging operator  $\pi_I$  to (13) that precludes volumetric locking without introducing additional degrees of freedom<sup>1</sup>. This

<sup>1</sup>The nodal averaging operator permits to integrate the weak form integrals directly at the nodes. This results in a total number of incompressibility constraints equal to the number of nodes in the mesh. If this number divides the total number of displacement equations, two degrees of freedom every one constraint is obtained in two dimensions, which is the optimal ratio to perform well in incompressible and nearly incompressible settings [65].

leads to a nodal version of (13), as follows: find  $\mathbf{u}_h \in \mathcal{V}_h$  such that

$$\begin{aligned} & \sum_{I \in \mathcal{T}_h} \left[ a_I(\pi_I[\Pi \mathbf{u}_h], \pi_I[\Pi \mathbf{v}_h]) + s_I(\pi_I[\mathbf{u}_h - \Pi \mathbf{u}_h], \pi_I[\mathbf{v}_h - \Pi \mathbf{v}_h]) \right] \\ & = \sum_{I \in \mathcal{T}_h} \ell_I(\pi_I[\Pi \mathbf{v}_h]) \quad \forall \mathbf{v}_h \in \mathcal{V}_h, \end{aligned} \quad (14)$$

where the notations  $a_I$ ,  $s_I$  and  $\ell_I$  are introduced as the nodal counterparts of  $a_E$ ,  $s_E$  and  $\ell_E$ , respectively. The construction of the nodal averaging operator is described next.

Each node of the mesh is associated with their own patch of virtual elements. The patch for node  $I$  is denoted by  $\mathcal{T}_I$  and is defined as the set of virtual elements connected to node  $I$  (see Fig. 2). Each node of a virtual element  $E$  in the patch is assigned the area  $\frac{1}{N_E}|E|$ ; that is, the area of an element is uniformly distributed among its nodes. The representative area of node  $I$  is denoted by  $|I|$  and is computed by addition of all the areas that are assigned to node  $I$  from the elements in  $\mathcal{T}_I$ ; that is,

$$|I| = \sum_{E \in \mathcal{T}_I} \frac{1}{N_E}|E|. \quad (15)$$

Similarly, each node of a virtual element  $E$  is uniformly assigned the strain  $\frac{1}{N_E}\widehat{\boldsymbol{\varepsilon}}(\mathbf{u}_h)$ . On considering each strain assigned to node  $I$  from the elements in  $\mathcal{T}_I$ , the *node-based uniform strain* is defined as follows:

$$\widehat{\boldsymbol{\varepsilon}}_I(\mathbf{u}_h) = \frac{1}{|I|} \sum_{E \in \mathcal{T}_I} |E| \frac{1}{N_E} \widehat{\boldsymbol{\varepsilon}}(\mathbf{u}_h). \quad (16)$$

Since  $\widehat{\boldsymbol{\varepsilon}}(\mathbf{u}_h)$  is by definition given at the element level, then from (16) the following nodal averaging operator is proposed:

$$\pi_I[\cdot] = \frac{1}{|I|} \sum_{E \in \mathcal{T}_I} |E| \frac{1}{N_E} [\cdot]_E, \quad (17)$$

where  $[\cdot]_E$  denotes evaluation over the element  $E$ .

### 2.3 NVEM nodal stiffness matrix and nodal force vector

The NVEM nodal stiffness matrix is developed by substituting the discretizations (3), the projection operator (8) and the nodal averaging operator (17) into the left-hand side of (14) for a node  $I$ . This gives

$$a_I(\pi_I[\Pi \mathbf{u}_h], \pi_I[\Pi \mathbf{v}_h]) + s_I(\pi_I[\mathbf{u}_h - \Pi \mathbf{u}_h], \pi_I[\mathbf{v}_h - \Pi \mathbf{v}_h]) = \mathbf{q}^\top \mathbf{K}_I \mathbf{d}, \quad (18)$$

where  $\mathbf{d}$  and  $\mathbf{q}$  are column vectors of element nodal displacements and element nodal values associated with  $\mathbf{v}_h$ , respectively;  $\mathbf{K}_I$  is the NVEM nodal stiffness matrix given

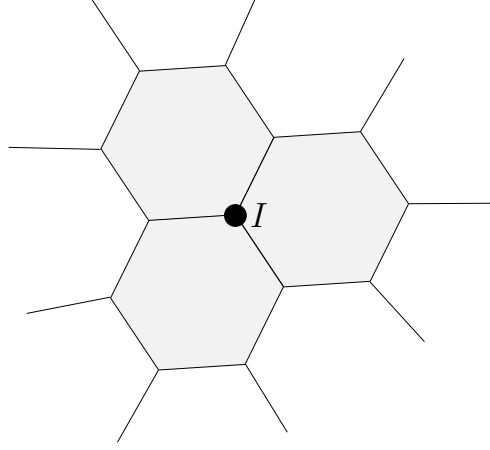


**Fig. 2:** Nodal patch  $\mathcal{T}_I$  (shaded elements) formed by the virtual elements that are connected to node  $I$

by

$$\mathbf{K}_I = \mathbf{K}_I^c + \mathbf{K}_I^s, \quad \mathbf{K}_I^c = |\mathbf{I}| \mathbf{B}_I^\top \mathbf{D} \mathbf{B}_I, \quad \mathbf{K}_I^s = (\mathbf{I} - \mathbf{P})_I^\top \mathbf{S} (\mathbf{I} - \mathbf{P})_I, \quad (19)$$

where  $\mathbf{D}$  is the constitutive matrix and  $\mathbf{S}$  is the stability matrix both defined in Section 3;  $\mathbf{B}_I = \pi_I[\mathbf{B}]$  and  $(\mathbf{I} - \mathbf{P})_I = \pi_I[\mathbf{I} - \mathbf{P}]$ , where  $\mathbf{I}$  is the identity ( $2N_E^V \times 2N_E^V$ ) matrix, and  $\mathbf{B}$  and  $\mathbf{P}$  are defined as

$$\mathbf{B} = \begin{bmatrix} \mathbf{B}_1 & \cdots & \mathbf{B}_a & \cdots & \mathbf{B}_{N_E^V} \end{bmatrix}, \quad \mathbf{B}_a = \begin{bmatrix} q_{1a} & 0 \\ 0 & q_{2a} \\ q_{2a} & q_{1a} \end{bmatrix}, \quad (20)$$

where  $q_{ia} = \frac{1}{|E|} \int_{\partial E} \phi_a(\mathbf{x}) n_i ds$  and can be exactly computed on the element boundary using a trapezoidal rule giving the following algebraic expression:

$$q_{ia} = \frac{1}{2|E|} (|e_{a-1}| n_{i(a-1)} + |e_a| n_{ia}), \quad i = 1, 2, \quad (21)$$

where  $n_{ia}$  is the  $i$ -th component of  $\mathbf{n}_a$  and  $|e_a|$  is the length of the edge incident to node  $a$  as defined in Fig. 1;

$$\mathbf{P} = \mathbf{H} \mathbf{B} + \mathbf{G} \mathbf{R}, \quad (22)$$

where

$$\mathbf{H} = \begin{bmatrix} \mathbf{H}_1 & \cdots & \mathbf{H}_a & \cdots & \mathbf{H}_{N_E^V} \end{bmatrix}^\top, \quad \mathbf{H}_a = \begin{bmatrix} (x_{1a} - \bar{x}_1) & 0 \\ 0 & (x_{2a} - \bar{x}_2) \\ \frac{1}{2}(x_{2a} - \bar{x}_2) & \frac{1}{2}(x_{1a} - \bar{x}_1) \end{bmatrix}^\top; \quad (23)$$

$$\mathbf{G} = \left[ \mathbf{G}_1 \cdots \mathbf{G}_a \cdots \mathbf{G}_{N_E^V} \right]^T, \quad \mathbf{G}_a = \begin{bmatrix} 1 & 0 \\ 0 & 1 \\ \frac{1}{2}(x_{2a} - \bar{x}_2) & \frac{1}{2}(\bar{x}_1 - x_{1a}) \end{bmatrix}^T; \quad (24)$$

and

$$\mathbf{R} = \left[ \mathbf{R}_1 \cdots \mathbf{R}_a \cdots \mathbf{R}_{N_E^V} \right], \quad \mathbf{R}_a = \begin{bmatrix} \frac{1}{N_E^V} & 0 \\ 0 & \frac{1}{N_E^V} \\ q_{2a} & -q_{1a} \end{bmatrix}. \quad (25)$$

Similarly, the NVEM nodal force vector is developed using the right-hand side of (14) for a node  $I$ , which leads to

$$\ell_I(\pi_I[II\mathbf{v}_h]) = \mathbf{q}^T \mathbf{f}_I, \quad (26)$$

where  $\mathbf{q}$  is the column vector of element nodal values associated with  $\mathbf{v}_h$ , and  $\mathbf{f}_I$  is the NVEM nodal force vector associated with the body force and external tractions defined as

$$\mathbf{f}_I = \mathbf{f}_I^b + \mathbf{f}_I^t, \quad \mathbf{f}_I^b = |I| \bar{\mathbf{N}}_I^T \hat{\mathbf{b}}_I, \quad \mathbf{f}_I^t = |I_\Gamma| \bar{\mathbf{N}}_{\Gamma,I}^T \hat{\mathbf{t}}_{N,I}. \quad (27)$$

For computing the nodal body force vector  $\mathbf{f}_I^b$  in (27),  $\bar{\mathbf{N}}_I = \pi_I[\bar{\mathbf{N}}]$  and  $\hat{\mathbf{b}}_I = \pi_I[\hat{\mathbf{b}}]$ , where

$$\bar{\mathbf{N}} = \left[ \bar{\mathbf{N}}_1 \cdots \bar{\mathbf{N}}_a \cdots \bar{\mathbf{N}}_{N_E^V} \right], \quad \bar{\mathbf{N}}_a = \begin{bmatrix} \frac{1}{N_E^V} & 0 \\ 0 & \frac{1}{N_E^V} \end{bmatrix}; \quad (28)$$

and

$$\hat{\mathbf{b}} = \frac{1}{|E|} \int_E \mathbf{b} \, dx. \quad (29)$$

Regarding the nodal traction force vector  $\mathbf{f}_I^t$  in (27), the nodal components are now computed with respect to the one-dimensional domain on the Neumann boundary; that is, the representative nodal area reduces to a representative nodal length  $|I_\Gamma| = \sum_{e \in \mathcal{T}_I} \frac{1}{2}|e|$ , where  $e$  is an element's edge located on the Neumann boundary and  $|e|$  its length;  $\mathcal{T}_I$  now represents the set of edges connected to node  $I$  on the Neumann boundary. Using the preceding definitions, the nodal averaging operator on the Neumann boundary is defined as

$$\pi_{I,\Gamma}[\cdot] = \frac{1}{|I_\Gamma|} \sum_{e \in \mathcal{T}_I} |e| \frac{1}{2} [\cdot]_e, \quad (30)$$

where  $[\cdot]_e$  denotes evaluation over the edge  $e$ . The remainder nodal matrices are then obtained as  $\bar{\mathbf{N}}_{\Gamma,I} = \pi_{I,\Gamma}[\bar{\mathbf{N}}_\Gamma]$  and  $\hat{\mathbf{t}}_{N,I} = \pi_{I,\Gamma}[\hat{\mathbf{t}}_N]$ , where

$$\bar{\mathbf{N}}_\Gamma = \begin{bmatrix} \frac{1}{2} & 0 & \frac{1}{2} & 0 \\ 0 & \frac{1}{2} & 0 & \frac{1}{2} \end{bmatrix}, \quad (31)$$

and

$$\widehat{\mathbf{t}}_N = \frac{1}{|e|} \int_e \mathbf{t}_N ds. \quad (32)$$

## 2.4 NVEM equilibrium equations for elastoplasticity

For linear elastostatics as developed in Ref. [60], the discrete equilibrium equation is obtained by the discretization of (14). This is accomplished by summing (18) and (26) through all the nodes in the domain and invoking the arbitrariness of  $\mathbf{q}$ . This results in the following system of equations:

$$\sum_{I \in \mathcal{T}_h} \left[ |I| \mathbf{B}_I^\top \mathbf{D} \mathbf{B}_I + (\mathbf{I} - \mathbf{P})_I^\top \mathbf{S} (\mathbf{I} - \mathbf{P})_I \right] \mathbf{d} = \sum_{I \in \mathcal{T}_h} \mathbf{f}_I. \quad (33)$$

Eq. (33) is also the discrete equilibrium equation for elastoplasticity when  $\mathbf{D}$  and  $\mathbf{S}$  are nonlinear functions obtained from the elastoplastic constitutive law. As usual, the solution for this problem requires the linearization of (33). Doing this gives

$$\begin{aligned} & \sum_{I \in \mathcal{T}_h} \left[ |I| \mathbf{B}_I^\top \check{\mathbf{D}}^{ep} \mathbf{B}_I + (\mathbf{I} - \mathbf{P})_I^\top \check{\mathbf{S}} (\mathbf{I} - \mathbf{P})_I \right] \Delta \mathbf{d} \\ & = - \sum_{I \in \mathcal{T}_h} \left[ |I| \mathbf{B}_I^\top \check{\boldsymbol{\sigma}} + (\mathbf{I} - \mathbf{P})_I^\top \check{\mathbf{S}} (\mathbf{I} - \mathbf{P})_I \mathbf{d} - \mathbf{f}_I \right], \end{aligned} \quad (34)$$

where  $\check{\mathbf{D}}^{ep}$ ,  $\check{\mathbf{S}}$ , and  $\check{\boldsymbol{\sigma}}$ , which are given in Section 3, are the elastoplastic consistent tangent operator, the stability matrix, and the nonlinear stress, respectively, evaluated at node  $I$  (by means of the elastoplastic constitutive law) using the node-based uniform strain  $\widehat{\boldsymbol{\varepsilon}}_I$ .

The linearized equilibrium equation (34) is used to solve the equilibrium state  $\mathbf{d}_{n+1}^{(k)} = \mathbf{d}_{n+1}^{(k-1)} + \Delta \mathbf{d}^{(k)}$  at time  $t_{n+1}$  with a time increment  $\Delta t = t_{n+1} - t_n$  via Newton-Raphson iterations, as follows:

$$\sum_{I \in \mathcal{T}_h} \left[ \mathbf{K}_{I,T}^c + \mathbf{K}_{I,T}^s \right]_{n+1}^{(k-1)} \Delta \mathbf{d}^{(k)} = - \sum_{I \in \mathcal{T}_h} \left[ \mathbf{f}_I^c + \mathbf{f}_I^s - \mathbf{f}_I \right]_{n+1}^{(k-1)}, \quad (35)$$

where

$$\begin{aligned} \mathbf{K}_{I,T}^c &= |I| \mathbf{B}_I^\top \check{\mathbf{D}}^{ep} \mathbf{B}_I, \quad \mathbf{K}_{I,T}^s = (\mathbf{I} - \mathbf{P})_I^\top \check{\mathbf{S}} (\mathbf{I} - \mathbf{P})_I, \\ \mathbf{f}_I^c &= |I| \mathbf{B}_I^\top \check{\boldsymbol{\sigma}}, \quad \mathbf{f}_I^s = (\mathbf{I} - \mathbf{P})_I^\top \check{\mathbf{S}} (\mathbf{I} - \mathbf{P})_I \mathbf{d}. \end{aligned} \quad (36)$$

## 3 Elastoplastic constitutive model and stabilization

Within the standard VEM framework, stabilization is one of the key ingredients for convergence of the method. However, in nodal integration, stabilization can make the formulation somewhat stiff in incompressible settings [8]. Therefore, the stabilization

in any nodal integration scheme, which includes the NVEM, must be cautiously chosen to not jeopardize its locking-free essence. To deal with this issue, we propose a *D-recipe* stabilization [66, 67] that uses only a deviatoric term. Firstly, a summary of the constitutive model considered for the elastoplastic solid is given and, secondly, the stabilization for the NVEM is detailed.

### 3.1 Constitutive model

The strain tensor  $\boldsymbol{\varepsilon}$  is split into elastic ( $\boldsymbol{\varepsilon}^e$ ) and plastic ( $\boldsymbol{\varepsilon}^p$ ) parts; that is,

$$\boldsymbol{\varepsilon} = \boldsymbol{\varepsilon}^e + \boldsymbol{\varepsilon}^p. \quad (37)$$

The elastic part is governed by the standard linear elastic law, and the plastic part by the von Mises model with mixed linear hardening (for details on this model, see for instance Ref. [68]). The yield function for this model is

$$\Phi(\boldsymbol{\sigma}, \boldsymbol{\beta}, \sigma_y) = \sqrt{3 J_2(\boldsymbol{s}(\boldsymbol{\sigma}) - \boldsymbol{\beta})} - \sigma_y(\bar{\boldsymbol{\varepsilon}}^p) = \sqrt{\frac{3}{2}} \|\boldsymbol{\eta}\| - \sigma_y(\bar{\boldsymbol{\varepsilon}}^p), \quad (38)$$

where  $\boldsymbol{\beta}$  is the backstress tensor,  $\sigma_y$  is a function of the accumulated plastic strain  $\bar{\boldsymbol{\varepsilon}}^p$  and defines the radius of the yield surface, and  $\boldsymbol{\eta}$  is the relative stress given by

$$\boldsymbol{\eta} = \boldsymbol{s} - \boldsymbol{\beta}, \quad (39)$$

where  $\boldsymbol{s}$  is the deviatoric stress. The plastic flow is described by the following associative law:

$$\dot{\boldsymbol{\varepsilon}}^p = \dot{\gamma} \sqrt{\frac{3}{2}} \frac{\boldsymbol{\eta}}{\|\boldsymbol{\eta}\|}, \quad (40)$$

where  $\dot{\boldsymbol{\varepsilon}}^p$  is the rate of the plastic strain tensor and  $\dot{\gamma}$  is the plastic multiplier.

The mixed linear hardening combines linear isotropic and linear kinematic hardening models. The linear isotropic hardening model is defined by the linear function

$$\sigma_y(\bar{\boldsymbol{\varepsilon}}^p) = \sigma_{y0} + H_i \bar{\boldsymbol{\varepsilon}}^p, \quad (41)$$

where  $\sigma_{y0}$  is the initial yield stress and  $H_i$  is the linear isotropic hardening modulus. The linear kinematic hardening model describes the evolution law for the backstress as the following linear function:

$$\dot{\boldsymbol{\beta}} = \frac{2}{3} H_k \dot{\boldsymbol{\varepsilon}}^p, \quad (42)$$

where  $H_k$  is the linear kinematic hardening modulus.

Let  $n$  and  $n + 1$  be the subindices that denote the previous and current states, respectively. These subindices are used for labeling the time at which the variables that are involved in the constitutive law are evaluated. Using the preceding notation,

the elastoplastic consistent tangent operator (in Voigt notation) for the above model is

$$\begin{aligned} \mathbf{D}_{n+1}^{ep} = & 2G \left( 1 - \frac{\Delta\gamma 3G}{\bar{q}_{n+1}^{\text{trial}}} \right) \mathbf{I}_d + 6G^2 \left( \frac{\Delta\gamma}{\bar{q}_{n+1}^{\text{trial}}} - \frac{1}{3G + H_k + H_i} \right) \bar{\mathbf{N}}_{n+1} \bar{\mathbf{N}}_{n+1}^\top \\ & + K \mathbf{m} \mathbf{m}^\top, \end{aligned} \quad (43)$$

where  $G$  and  $K$  are the shear modulus and bulk modulus of the material, respectively. Here, we use the three-dimensional constitutive law from where the plain strain state components are extracted. The remainder quantities that appear in (43) are defined as follows:

$$\mathbf{I}_d = \begin{bmatrix} 1 & 0 & 0 & 0 & 0 & 0 \\ 0 & 1 & 0 & 0 & 0 & 0 \\ 0 & 0 & 1 & 0 & 0 & 0 \\ 0 & 0 & 0 & 0.5 & 0 & 0 \\ 0 & 0 & 0 & 0 & 0.5 & 0 \\ 0 & 0 & 0 & 0 & 0 & 0.5 \end{bmatrix} - \frac{1}{3} \mathbf{m} \mathbf{m}^\top, \quad \mathbf{m} = \begin{bmatrix} 1 & 1 & 1 & 0 & 0 & 0 \end{bmatrix}^\top; \quad (44)$$

$$\bar{q}_{n+1}^{\text{trial}} = \sqrt{\frac{3}{2}} \|\boldsymbol{\eta}_{n+1}^{\text{trial}}\|, \quad \boldsymbol{\eta}_{n+1}^{\text{trial}} = \mathbf{s}_{n+1}^{\text{trial}} - \boldsymbol{\beta}_n, \quad (45)$$

$$\mathbf{s}_{n+1}^{\text{trial}} = 2G \left( \boldsymbol{\varepsilon}_{n+1}^{e \text{ trial}} - \frac{1}{3} \text{trace}(\boldsymbol{\varepsilon}_{n+1}^{e \text{ trial}}) \mathbf{m} \right), \quad \boldsymbol{\varepsilon}_{n+1}^{e \text{ trial}} = \boldsymbol{\varepsilon}_{n+1} - \boldsymbol{\varepsilon}_n^p;$$

$$\Delta\gamma = \frac{\Phi^{\text{trial}}}{3G + H_k + H_i}, \quad \Phi^{\text{trial}} = \bar{q}_{n+1}^{\text{trial}} - \sigma_y(\bar{\varepsilon}_{n+1}^p \text{ trial}), \quad \bar{\varepsilon}_{n+1}^p \text{ trial} = \bar{\varepsilon}_n^p; \quad (46)$$

$$\bar{\mathbf{N}}_{n+1} = \frac{\boldsymbol{\eta}_{n+1}^{\text{trial}}}{\|\boldsymbol{\eta}_{n+1}^{\text{trial}}\|}. \quad (47)$$

The strain/stress update is performed as follows:

$$\begin{aligned} \bar{\varepsilon}_{n+1}^p &= \bar{\varepsilon}_n^p + \Delta\gamma, \quad \boldsymbol{\varepsilon}_{n+1}^p = \boldsymbol{\varepsilon}_n^p + \Delta\gamma \sqrt{\frac{3}{2}} \bar{\mathbf{N}}_{n+1}, \\ \boldsymbol{\beta}_{n+1} &= \boldsymbol{\beta}_n + \Delta\gamma \sqrt{\frac{2}{3}} H_k \bar{\mathbf{N}}_{n+1}, \\ \mathbf{s}_{n+1} &= \mathbf{s}_{n+1}^{\text{trial}} - 2G \Delta\gamma \sqrt{\frac{3}{2}} \bar{\mathbf{N}}_{n+1}, \\ \boldsymbol{\sigma}_{n+1} &= \mathbf{s}_{n+1} + K \text{trace}(\boldsymbol{\varepsilon}_{n+1}^{e \text{ trial}}) \mathbf{m}. \end{aligned} \quad (48)$$

As previously mentioned in Section 2.4, in the NVEM the constitutive law is evaluated using the nodal strain  $\hat{\boldsymbol{\varepsilon}}_I$ ; that is, in (36),  $\check{\mathbf{D}}^{ep} = \mathbf{D}^{ep}(\boldsymbol{\varepsilon} = \hat{\boldsymbol{\varepsilon}}_I)$  and  $\check{\boldsymbol{\sigma}} = \boldsymbol{\sigma}(\boldsymbol{\varepsilon} = \hat{\boldsymbol{\varepsilon}}_I)$ .

The above computations of the elastoplastic consistent tangent operator and strain/stress update are part of the implicit elastic predictor/return mapping algorithm for numerical integration of the von Mises model with mixed linear hardening [68]. This algorithm is summarized in Algorithm 1.

---

**Algorithm 1** Implicit elastic predictor/return mapping algorithm for the von Mises model with mixed linear hardening

---

**Input:**  $(\widehat{\boldsymbol{\varepsilon}}_I)_{n+1}$ ,  $\bar{\boldsymbol{\varepsilon}}_n^p$ ,  $\boldsymbol{\varepsilon}_n^p$ ,  $\boldsymbol{\beta}_n$

**Output:**  $\bar{\boldsymbol{\varepsilon}}_{n+1}^p$ ,  $\boldsymbol{\varepsilon}_{n+1}^p$ ,  $\boldsymbol{\beta}_{n+1}$ ,  $\check{\boldsymbol{\sigma}}_{n+1}$ ,  $\check{\boldsymbol{D}}_{n+1}^{ep}$

(Elastic predictor)

Set  $\boldsymbol{\varepsilon}_{n+1} = (\widehat{\boldsymbol{\varepsilon}}_I)_{n+1}$

$\boldsymbol{\varepsilon}_{n+1}^{e \text{ trial}} = \boldsymbol{\varepsilon}_{n+1} - \boldsymbol{\varepsilon}_n^p$

$\boldsymbol{s}_{n+1}^{\text{trial}} = 2G \left( \boldsymbol{\varepsilon}_{n+1}^{e \text{ trial}} - \frac{1}{3} \text{trace}(\boldsymbol{\varepsilon}_{n+1}^{e \text{ trial}}) \boldsymbol{m} \right)$

$\boldsymbol{\eta}_{n+1}^{\text{trial}} = \boldsymbol{s}_{n+1}^{\text{trial}} - \boldsymbol{\beta}_n$ ,  $\bar{q}_{n+1}^{\text{trial}} = \sqrt{\frac{3}{2}} \|\boldsymbol{\eta}_{n+1}^{\text{trial}}\|$

$\bar{\boldsymbol{\varepsilon}}_{n+1}^{p \text{ trial}} = \bar{\boldsymbol{\varepsilon}}_n^p$ ,  $\boldsymbol{\beta}_{n+1}^{\text{trial}} = \boldsymbol{\beta}_n$

(Elastic/plastic check and update state)

$\Phi^{\text{trial}} = \bar{q}_{n+1}^{\text{trial}} - \sigma_y(\bar{\boldsymbol{\varepsilon}}_{n+1}^{p \text{ trial}})$

**if**  $\Phi^{\text{trial}} \leq 0$  **then** (elastic state)

$\bar{\boldsymbol{\varepsilon}}_{n+1}^p = \bar{\boldsymbol{\varepsilon}}_{n+1}^{p \text{ trial}}$ ,  $\boldsymbol{\varepsilon}_{n+1}^p = \boldsymbol{\varepsilon}_n^p$

$\boldsymbol{\beta}_{n+1} = \boldsymbol{\beta}_{n+1}^{\text{trial}}$

$\boldsymbol{\sigma}_{n+1} = \boldsymbol{s}_{n+1}^{\text{trial}} + K \text{trace}(\boldsymbol{\varepsilon}_{n+1}^{e \text{ trial}}) \boldsymbol{m}$

$\boldsymbol{D}_{n+1}^{ep} = 2G\boldsymbol{I}_d + K\boldsymbol{m}\boldsymbol{m}^\top$

**else** (plastic corrector)

$\Delta\gamma = \frac{\Phi^{\text{trial}}}{3G+H_k+H_i}$ ,  $\bar{\boldsymbol{N}}_{n+1} = \frac{\boldsymbol{\eta}_{n+1}^{\text{trial}}}{\|\boldsymbol{\eta}_{n+1}^{\text{trial}}\|}$

$\bar{\boldsymbol{\varepsilon}}_{n+1}^p = \bar{\boldsymbol{\varepsilon}}_n^p + \Delta\gamma$ ,  $\boldsymbol{\varepsilon}_{n+1}^p = \boldsymbol{\varepsilon}_n^p + \Delta\gamma\sqrt{\frac{3}{2}}\bar{\boldsymbol{N}}_{n+1}$

$\boldsymbol{\beta}_{n+1} = \boldsymbol{\beta}_n + \Delta\gamma\sqrt{\frac{2}{3}}H_k\bar{\boldsymbol{N}}_{n+1}$

$\boldsymbol{s}_{n+1} = \boldsymbol{s}_{n+1}^{\text{trial}} - 2G\Delta\gamma\sqrt{\frac{3}{2}}\bar{\boldsymbol{N}}_{n+1}$

$\boldsymbol{\sigma}_{n+1} = \boldsymbol{s}_{n+1} + K \text{trace}(\boldsymbol{\varepsilon}_{n+1}^{e \text{ trial}}) \boldsymbol{m}$

$\boldsymbol{D}_{n+1}^{ep} = 2G \left( 1 - \frac{\Delta\gamma 3G}{\bar{q}_{n+1}^{\text{trial}}} \right) \boldsymbol{I}_d + 6G^2 \left( \frac{\Delta\gamma}{\bar{q}_{n+1}^{\text{trial}}} - \frac{1}{3G+H_k+H_i} \right) \bar{\boldsymbol{N}}_{n+1} \bar{\boldsymbol{N}}_{n+1}^\top + K\boldsymbol{m}\boldsymbol{m}^\top$

**end if**

$\check{\boldsymbol{\sigma}}_{n+1} = \boldsymbol{\sigma}_{n+1}$ ,  $\check{\boldsymbol{D}}_{n+1}^{ep} = \boldsymbol{D}_{n+1}^{ep}$

---

### 3.2 Stabilization

As mentioned before, some precautions must be taken to stabilize the NVEM so that the locking-free behavior of the nodal integration scheme is preserved. Thus, drawing inspiration from one of the possibilities already explored in Ref. [60], the stabilization issue in the NVEM for elastoplastic solids is dealt with a diagonal stability matrix

that uses only a deviatoric term, as follows:

$$(\check{\mathbf{S}})_{i,i} = \max \left( 1, \left[ |I| \mathbf{B}_I^\top \mathbf{D}_d^e \mathbf{B}_I \right]_{i,i} \right), \quad (49)$$

where  $\mathbf{D}_d^e$  is the deviatoric part of the elastic moduli and is given by

$$\mathbf{D}_d^e = 2G\mathbf{I}_d. \quad (50)$$

This choice performs very well in a variety of two-dimensional numerical tests and does not introduce any tuning parameter.

## 4 Numerical examples

In this section, some benchmark tests are conducted to demonstrate the performance of the NVEM in elastoplastic solids simulations. The method is compared with the well-known locking-free 9-node B-bar quadrilateral finite element [3] (FEM Q9 B-bar) as well as with the standard linearly precise virtual element (VEM) and in some cases with the standard 4-node quadrilateral finite element (FEM Q4). All the tests are conducted using the constitutive model described in Section 3.1. Throughout this section, DOF stands for degree(s) of freedom,  $E_Y$  is the Young's modulus,  $\nu$  is the Poisson's ratio,  $\sigma_{y0}$  is the initial yield stress, and  $H_i$  and  $H_k$  are the linear isotropic hardening modulus and the linear kinematic hardening modulus, respectively.

### 4.1 Thick-walled cylinder

In this test, the ability of the NVEM for solving compressible and nearly incompressible elastoplastic problems is demonstrated. The problem consists of a plane strain (unit thickness) representation of a thick-walled cylinder under internal pressure. The geometry, boundary conditions, and mesh used in this numerical test are shown in Fig. 3, where the internal pressure is  $p = 180$  MPa, and the internal and external radii are  $r_i = 100$  mm and  $r_o = 200$  mm, respectively. The material parameters used are the following:  $E_Y = 210000$  MPa,  $\nu = 0.3$  for the compressible case and  $\nu = 0.4999$  for the nearly incompressible case,  $\sigma_{y0} = 240$  MPa,  $H_i = H_k = 0$  MPa (perfect plasticity).

The radial displacement at points  $A$  and  $B$  for the compressible and nearly incompressible cases is summarized in Fig. 4 for all the methods. For the compressible case, all the methods match very well (Fig. 4(a)). On the other hand, for the nearly incompressible case (Fig. 4(b)), the NVEM and FEM Q9 B-bar methods still match very well, whereas the VEM and FEM Q4 clearly exhibit a locking behavior since radial displacements are smaller than expected. The same behaviors are observed in the total displacement (Fig. 5), pressure (Fig. 6), and von Mises stress (Fig. 7) field solutions at the last load step for the nearly incompressible case.

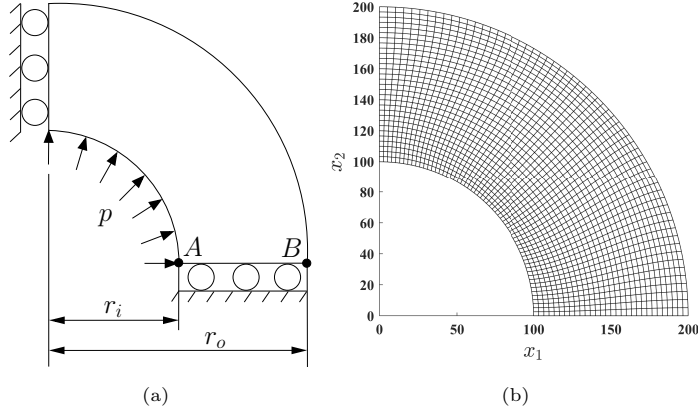


**Fig. 3:** Thick-walled cylinder problem. (a) Geometry and boundary conditions, and (b) mesh used for benchmarking the VEM, NVEM, FEM Q4 and FEM Q9 B-bar approaches

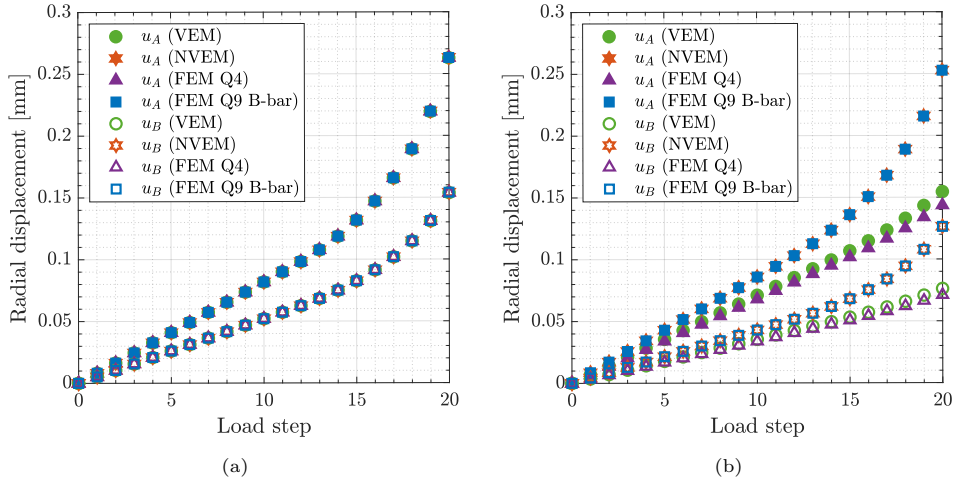


**Fig. 4:** Radial displacement at points  $A$  ( $u_A$ ) and  $B$  ( $u_B$ ) due to the applied internal pressure in steps for the thick-walled cylinder problem. (a) Compressible case ( $\nu = 0.3$ ), and (b) nearly incompressible case ( $\nu = 0.4999$ )

## 4.2 Cook's membrane

The next example consists of a tapered beam fixed along one end and loaded with a shear force at the other end. It is designed to study the performance of numerical formulations under combined bending and shear when the solid material behaves nearly incompressible. The geometry and boundary conditions are depicted in Fig. 8, where

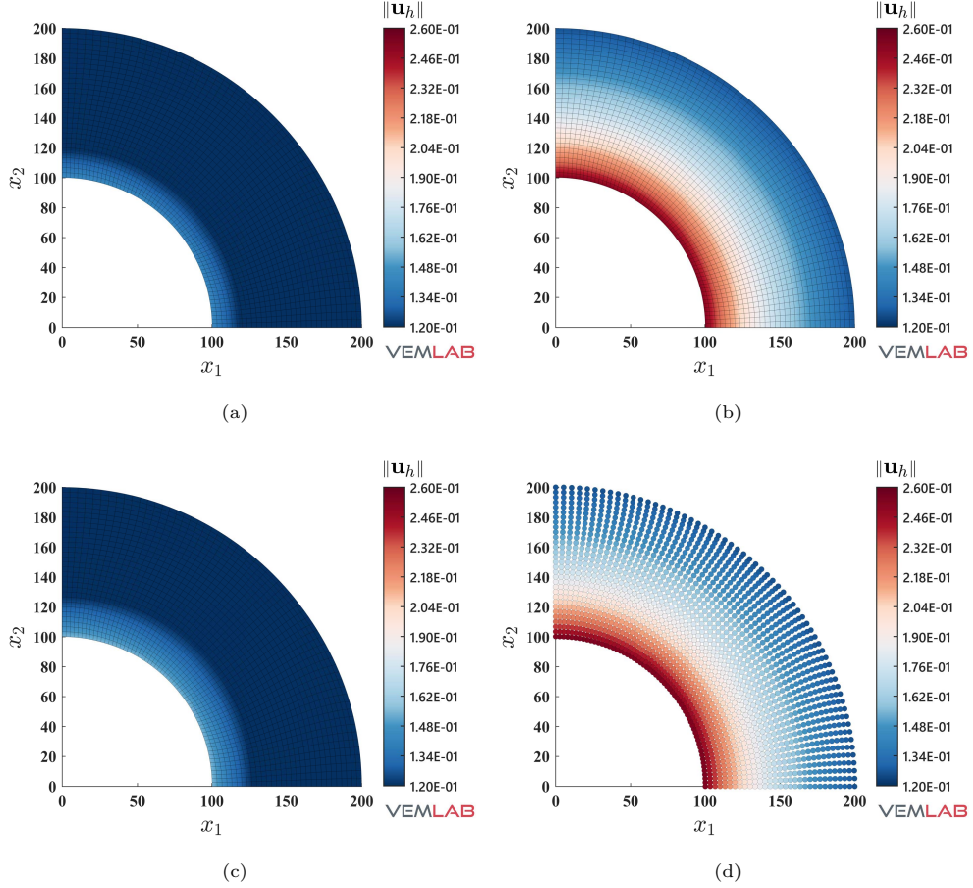


**Fig. 5:** Plots of the total displacement field solution in mm at the last load step for the nearly incompressible thick-walled cylinder problem ( $\nu = 0.4999$ ). (a) FEM Q4, (b) FEM Q9 B-bar, (c) VEM, and (d) NVEM

the shear load is  $F = 3.6$  N/mm (total shear load of 57.6 N). The beam has a unit thickness and plane strain condition is assumed. The following material parameters are used:  $E_Y = 1500$  MPa,  $\nu = 0.4999$ ,  $\sigma_{y0} = 7.5$  MPa,  $H_i = 3.25$  MPa, and  $H_k = 0$  MPa. In this test, the performance of the NVEM is compared with the VEM and the FEM Q9 B-bar. Sample meshes used in this test are shown in Fig. 9.

The convergence of the vertical displacement at the tip of the beam (point  $A$  in Fig. 8) upon mesh refinement is depicted in Fig. 10. As expected, the VEM solution exhibits a severe locking behavior, whereas the NVEM and FEM Q9 B-bar are locking-free and their solutions are in good agreement upon mesh refinement.

Fig. 11 depicts the pressure field and the von Mises stress field solutions on the most refined mesh for the NVEM and FEM Q9 B-bar approaches. The NVEM plots do not look as smooth as the FEM plots because of the particular shape of the polygonal

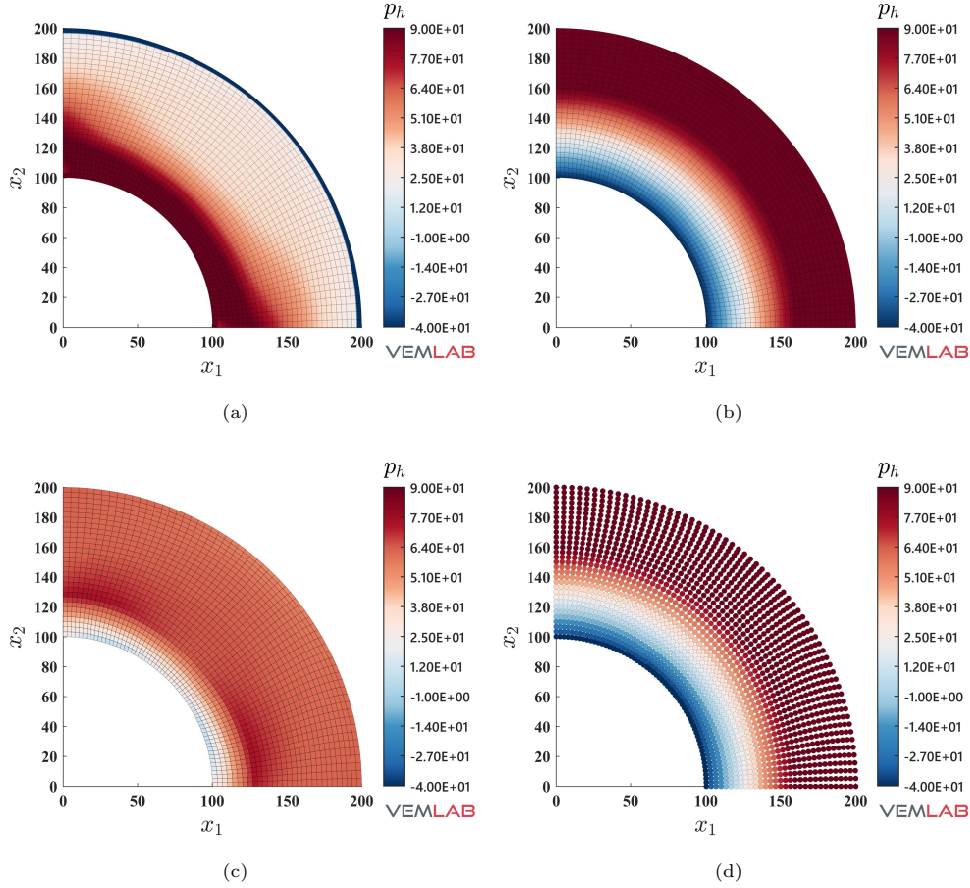
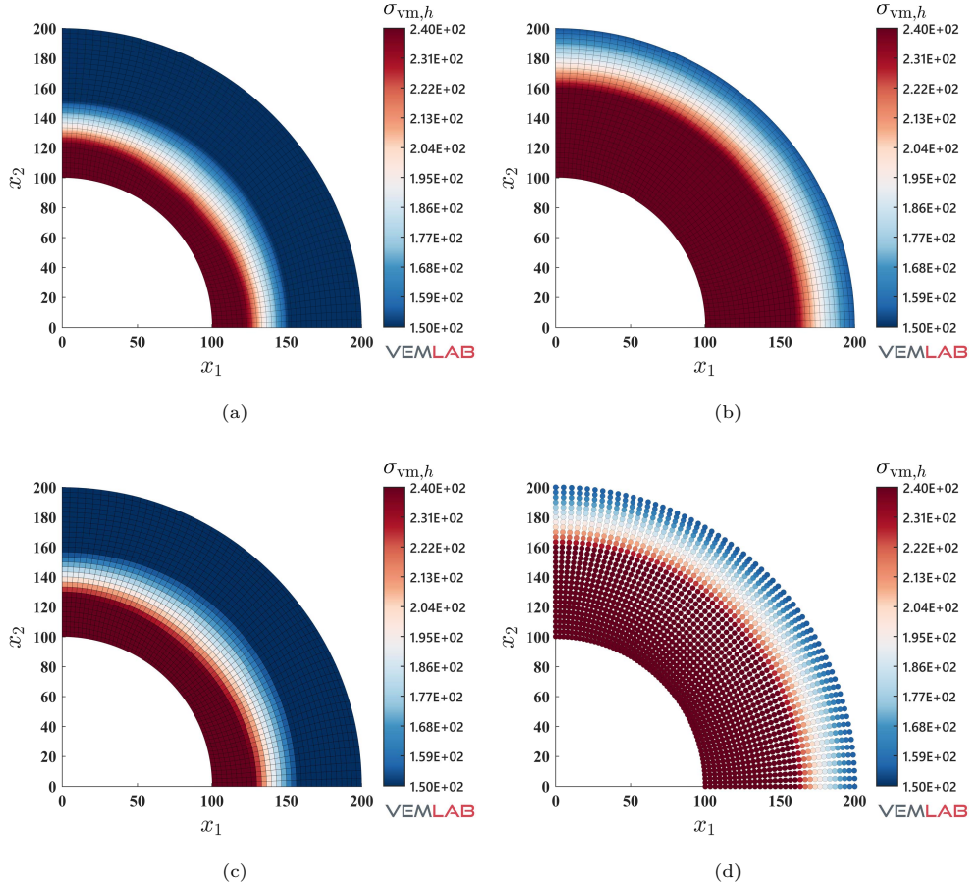


**Fig. 6:** Plots of the pressure field solution in MPa for the nearly incompressible thick-walled cylinder problem ( $\nu = 0.4999$ ). (a) FEM Q4, (b) FEM Q9 B-bar, (c) VEM, and (d) NVEM

element used to construct the mesh for the NVEM case (see Fig. 9(a)). Despite this, the solutions are in good agreement.

### 4.3 Tension problem

In this example, the performance of the NVEM is studied on a pure tension problem. The domain consists of a square of dimensions  $100 \times 100 \text{ mm}^2$  and unit thickness. Plane strain condition is specified and the following material parameters are used:  $E_Y = 200000 \text{ MPa}$ ,  $\nu = 0.4999$ ,  $\sigma_{y0} = 150 \text{ MPa}$ ,  $H_i = H_k = 0 \text{ MPa}$  (perfect plasticity). On the top edge of the domain, a vertical displacement of  $0.5 \text{ mm}$  is imposed while its lateral movement is restrained. The bottom surface of the domain is fixed. Fig. 12 summarizes the problem definition and presents the mesh used in the analysis.



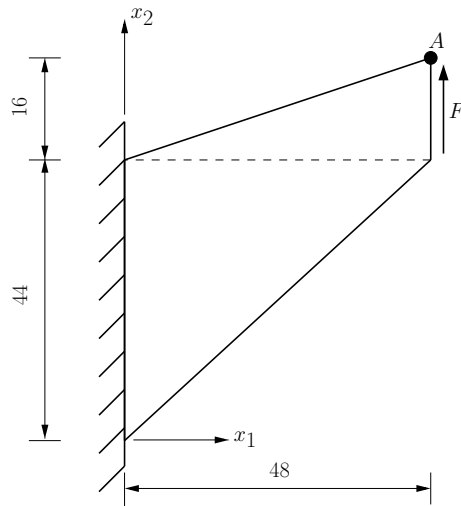
**Fig. 7:** Plots of the von Mises stress field solution in MPa for the nearly incompressible thick-walled cylinder problem ( $\nu = 0.4999$ ). (a) FEM Q4, (b) FEM Q9 B-bar, (c) VEM, and (d) NVEM

Fig. 13 presents the load-displacement curve, where a coincident limit load is observed for the NVEM and FEM Q9 B-bar approaches. On the other hand, the load-displacement curve for the VEM shows a locking effect both in the elastic and plastic regimes.

The solutions for the accumulated plastic strain and the von Mises stress are presented in Fig. 14, where once again good agreement is observed between the NVEM and FEM Q9 B-bar methods.

#### 4.4 Perforated plate

In this benchmark problem, a quarter of a perforated plate is considered. The geometry, boundary conditions, and sample mesh are depicted in Fig. 15. The plate has



**Fig. 8:** Geometry and boundary conditions for the Cook's membrane problem with dimensions in mm

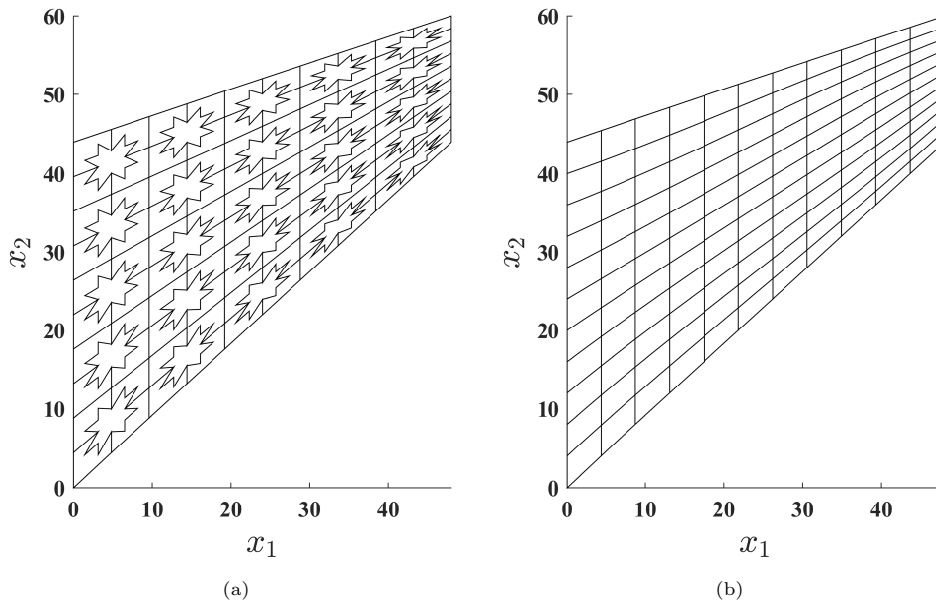


**Fig. 9:** Sample meshes for the Cook's membrane problem that are used in the (a) VEM and NVEM, and (b) FEM Q9 B-bar approaches

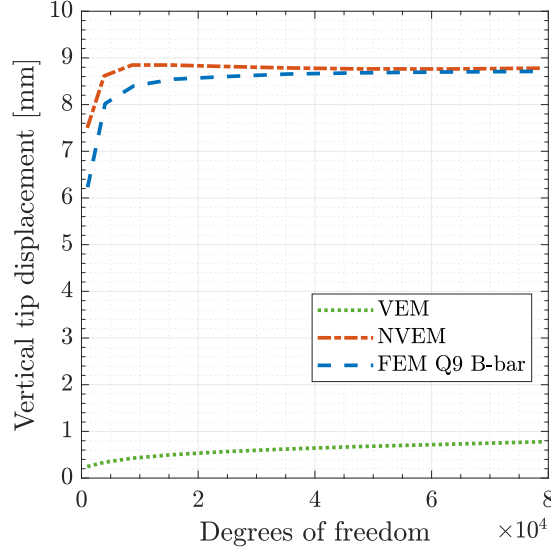


**Fig. 10:** Convergence of the vertical displacement at the tip of the Cook’s membrane (point A) upon mesh refinement

unit thickness and plane strain condition is assumed. The material parameters are set to  $E_Y = 68646.55$  MPa,  $\nu = 0.3$ ,  $\sigma_{y0} = 238.301595$  MPa,  $H_i = H_k = 0$  MPa (perfect plasticity). A vertical displacement  $u_{2D} = 2$  mm is applied on the top edge of the plate. On the left, right, and bottom edges of the plate, the translation is restrained in the normal direction to these edges. Therefore, the plate is highly constrained and thus a locking effect is expected for the standard linearly precise VEM. In fact, this is confirmed in the response curve shown in Fig. 16, where the expected limit load is achieved only by the NVEM and the FEM Q9 B-bar in the plastic regime. A pictorial of the accumulated plastic strain and the von Mises stress for the most refined mesh is shown in Fig. 17, where it is observed that the NVEM and FEM Q9 B-bar solutions look very similar.

A comparison of the horizontal displacement at point *A* and the vertical displacement at point *B* among the different methods is presented in Table 1, where a perfect match to three decimal places is obtained for the NVEM and FEM Q9 B-bar methods.

**Table 1:** Displacement comparison for the perforated plate problem

Method	$u_{1A}$ [mm]	$u_{2B}$ [mm]
VEM	2.716	1.850
NVEM	2.745	1.855
FEM Q4	2.714	1.849
FEM Q9 B-bar	2.745	1.855

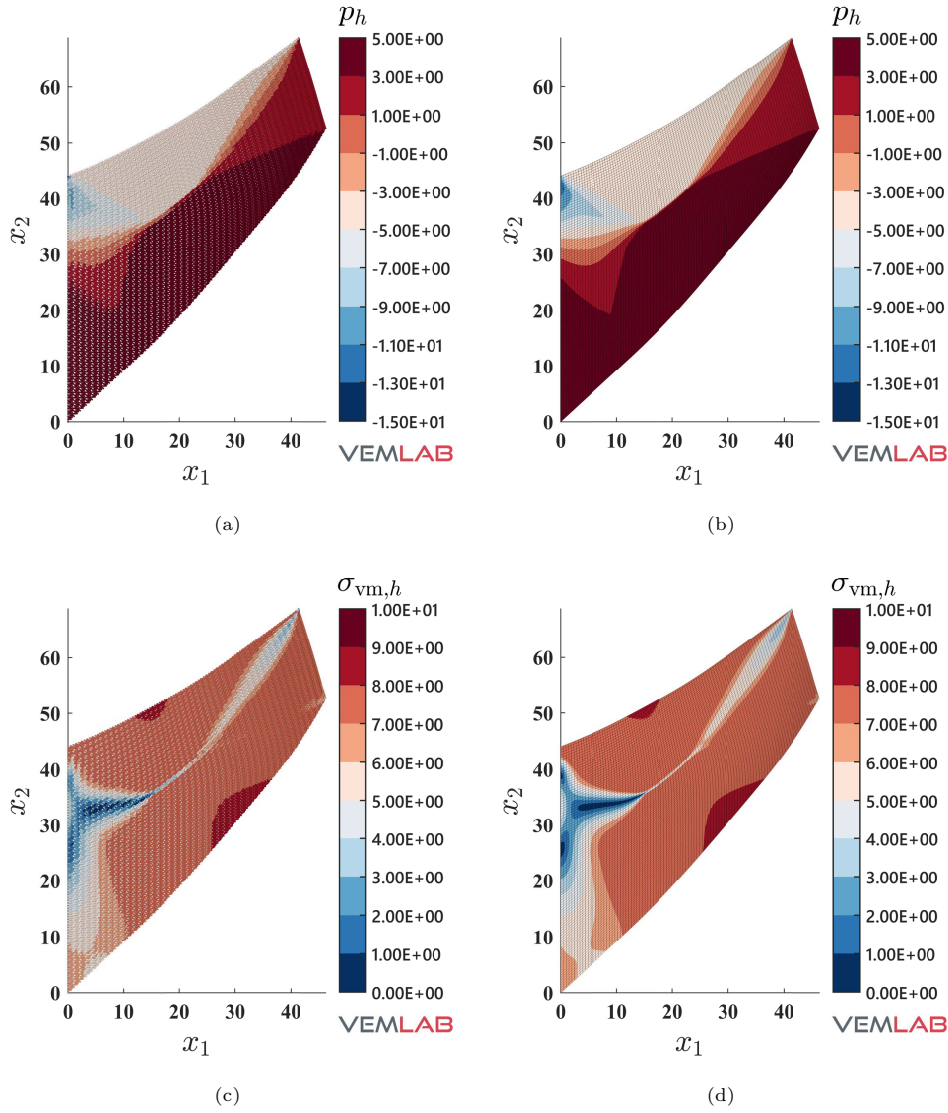


**Fig. 11:** Cook's membrane problem. Pressure field solution in MPa ((a) NVEM, (b) FEM Q9 B-bar), and von Mises stress field solution in MPa ((c) NVEM, (d) FEM Q9 B-bar)

## 4.5 Prandtl's punch test

The last benchmark problem is devoted to demonstrate the performance of the NVEM in a highly constrained compression problem. The Prandtl's punch test [69] is selected for this purpose. The geometry and boundary conditions are shown in Fig. 18, where

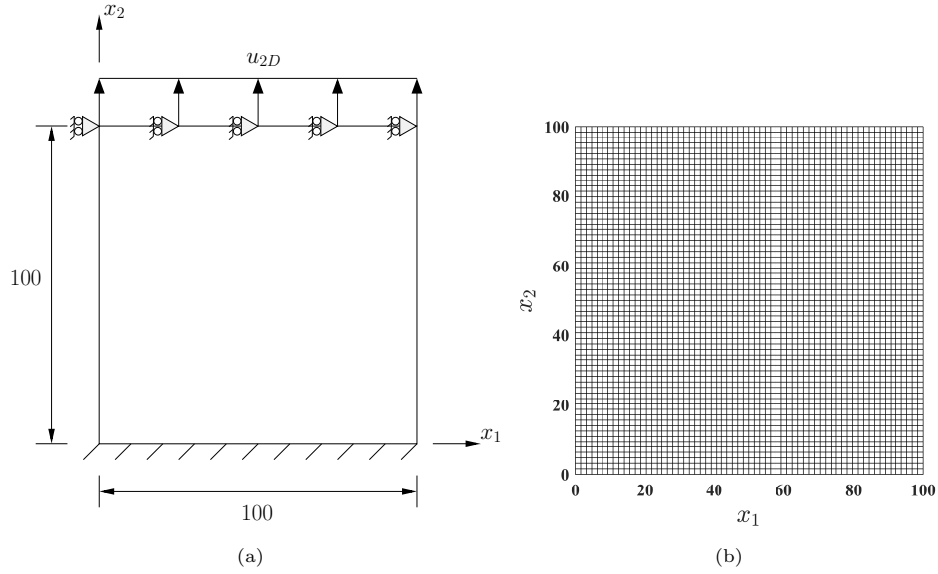


**Fig. 12:** Tension problem. (a) Geometry and boundary conditions, and (b) mesh used for benchmarking the VEM, NVEM, and FEM Q9 B-bar approaches

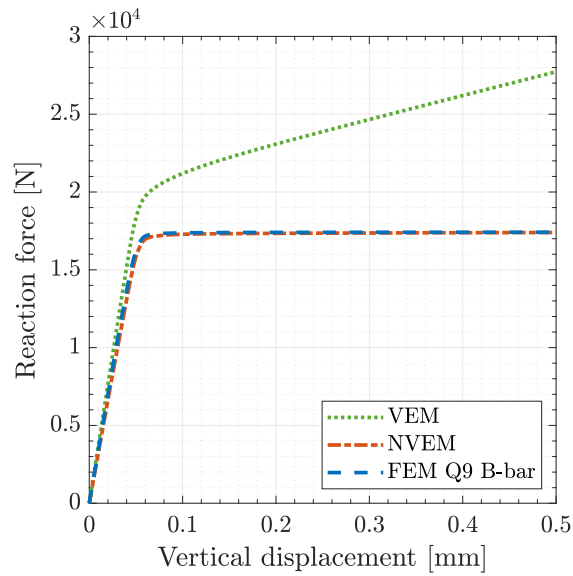


**Fig. 13:** Load-displacement curve for the tension problem

the punch surface located on the top is horizontally restrained (rough punch) while a downward vertical displacement  $u_{2D} = -50$  mm is imposed on it. The dimensions

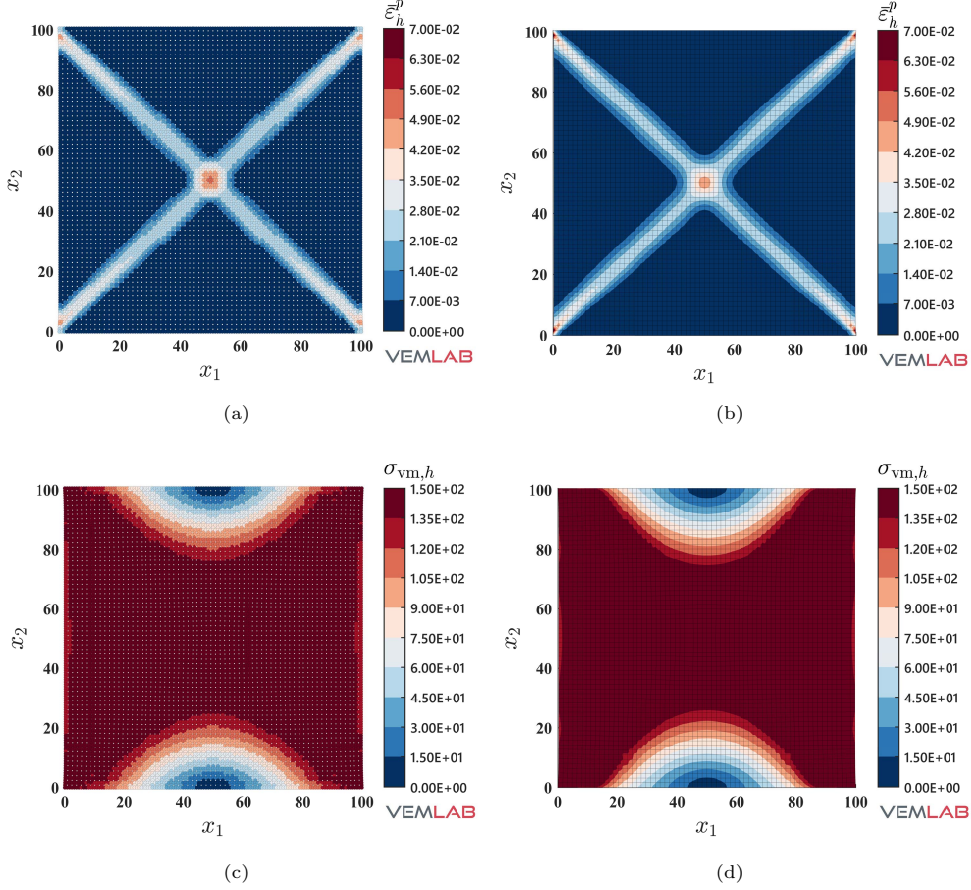


**Fig. 14:** Tension problem. Accumulated plastic strain field solution ((a) NVEM, (b) FEM Q9 B-bar), and von Mises stress field solution in MPa ((c) NVEM, (d) FEM Q9 B-bar)

are defined using  $a = 500$  mm. Because of the symmetry, only half of the domain is considered for discretization. Three polygonal meshes with increasing refinements are considered for the VEM and NVEM (Fig. 19(a)–(c)). The most refined VEM/NVEM mesh (Fig. 19(c)) and the mesh for the FEM Q9 B-bar (Fig. 19(d)) have similar number of DOF. Unit thickness is considered and plane strain condition is assumed with material parameters set to  $E_Y = 10^5$  MPa,  $\nu = 0.499$ ,  $\sigma_{y0} = E_Y/1000$  MPa,  $H_i = H_k = 0$  MPa (perfect plasticity). As observed in Fig. 20, a severe locking behavior is obtained for the standard linearly precise VEM in this highly constrained problem. On the other hand, the same figure reports the nearly coincident limit load that is obtained for the NVEM and FEM Q9 B-bar approaches. The accumulated plastic strain is reported on Fig. 21, where similar results are obtained for the NVEM and FEM Q9 B-bar on the meshes with similar number of DOF (Fig. 21(c) and Fig. 21(d),

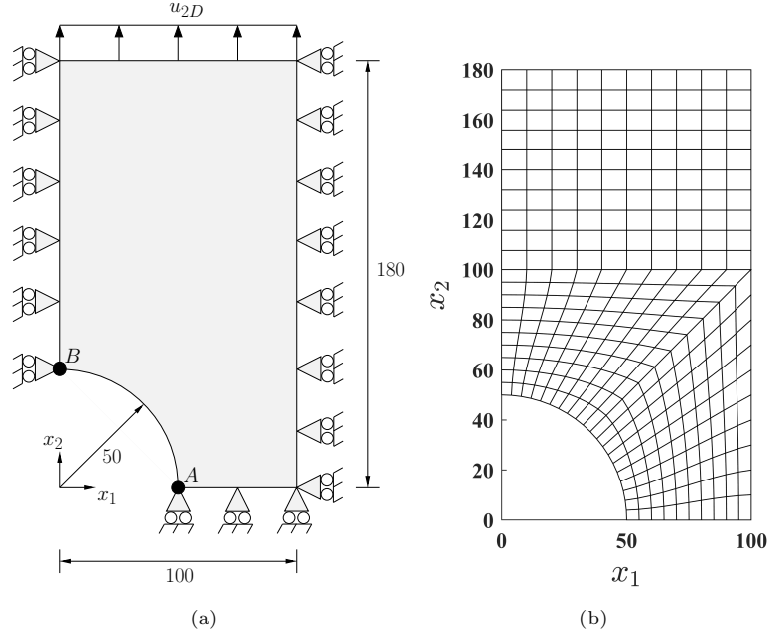


**Fig. 15:** Perforated plate problem. (a) Geometry (with dimensions in mm) and boundary conditions, and (b) a sample mesh used for benchmarking the VEM, NVEM, FEM Q4, and FEM Q9 B-bar approaches

respectively). The pressure field is depicted in Fig. 22, where the NVEM and FEM Q9 B-bar solutions look very similar and smooth on the meshes with similar number of DOF (Fig. 22(c) and Fig. 22(d), respectively). Just for completeness, the accumulated plastic strain and the pressure field solutions for the linearly precise VEM are shown in Fig. 23, where the severe locking behavior is clearly observed in the oscillations of the pressure field.

## 5 Summary and conclusions

The node-based uniform strain virtual element method (NVEM) that was recently proposed for compressible and nearly incompressible elasticity [60] has been extended to elastoplastic solids at small strains. In the proposed method, the strain is averaged at the nodes from the strain of surrounding linearly precise virtual elements using a generalization to virtual elements of the node-based uniform strain approach for finite elements [6]. The averaged strain is then used to sample the weak form at the nodes of the mesh leading to a method in which all the field variables, including state and history-dependent variables, are related to the nodes. Consequently, in the nonlinear computations these variables are tracked only at the nodal locations.

Various elastoplastic benchmark problems were conducted to assess the performance of the NVEM. These included a thick-walled cylinder under internal pressure,

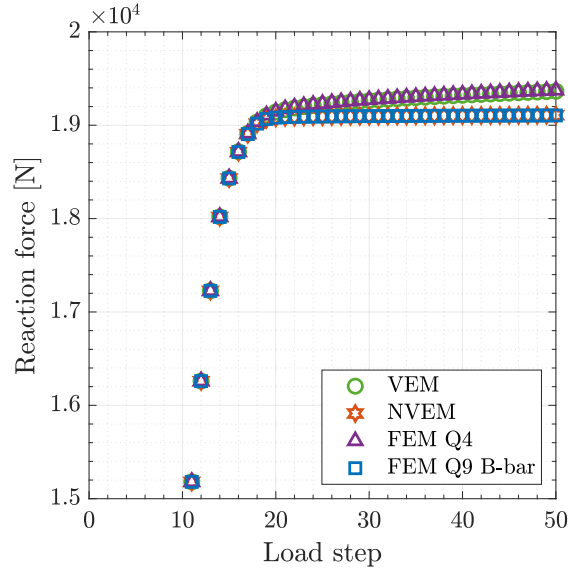


**Fig. 16:** Response curve for the perforated plate problem. Reaction force due to the applied vertical displacement in steps

a combined bending and shear problem (Cook’s membrane), a pure tension problem, a perforated plate subjected to a displacement producing tension, and a highly constrained problem in compression (Prandtl’s punch test). The comparisons with the well-known locking-free 9-node B-bar quadrilateral finite element [3] revealed that the NVEM effectively enables linearly precise virtual elements to solve elastoplastic solids with accuracy and is locking-free. For perfect plasticity, these comparisons also demonstrated that the NVEM is able to capture the expected limit load. Finally, we mention that the present work completes our short term scope for the NVEM development and that its extension to large deformations with remeshing is an undergoing work.

**Acknowledgements.** This work was performed under the auspices of the Chilean National Fund for Scientific and Technological Development (FONDECYT) through grant ANID FONDECYT No. 1221325 (R.S-V and A.O-B).

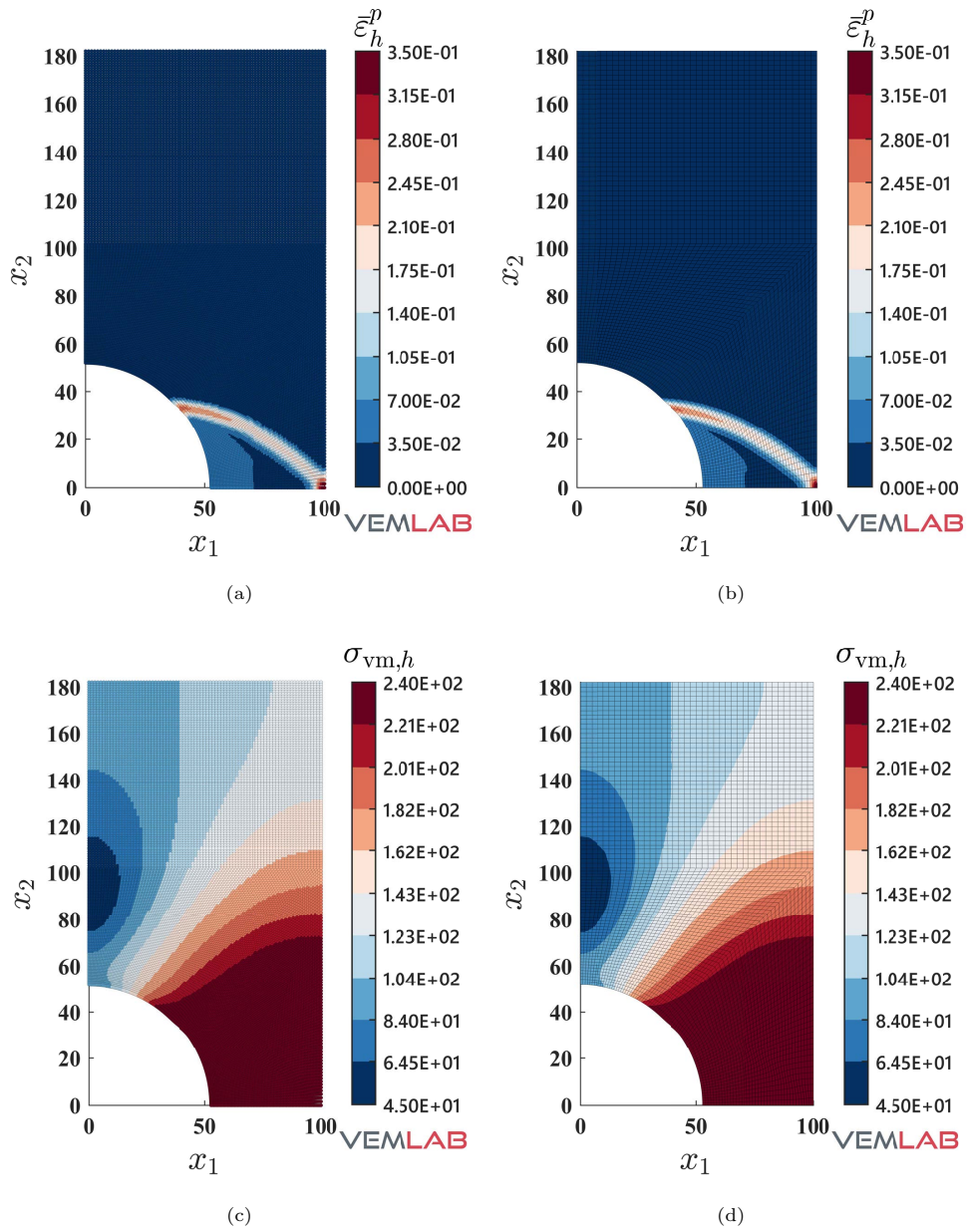


**Fig. 17:** Perforated plate problem. Accumulated plastic strain field solution ((a) NVEM, (b) FEM Q9 B-bar), and von Mises stress field solution in MPa ((c) NVEM, (d) FEM Q9 B-bar)

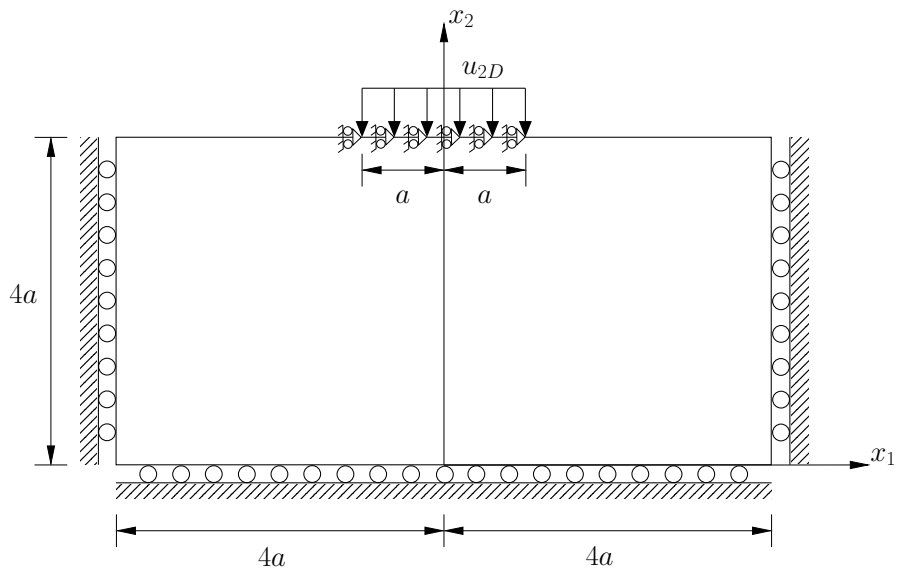


**Fig. 18:** Geometry and boundary conditions for the Prandtl's punch test

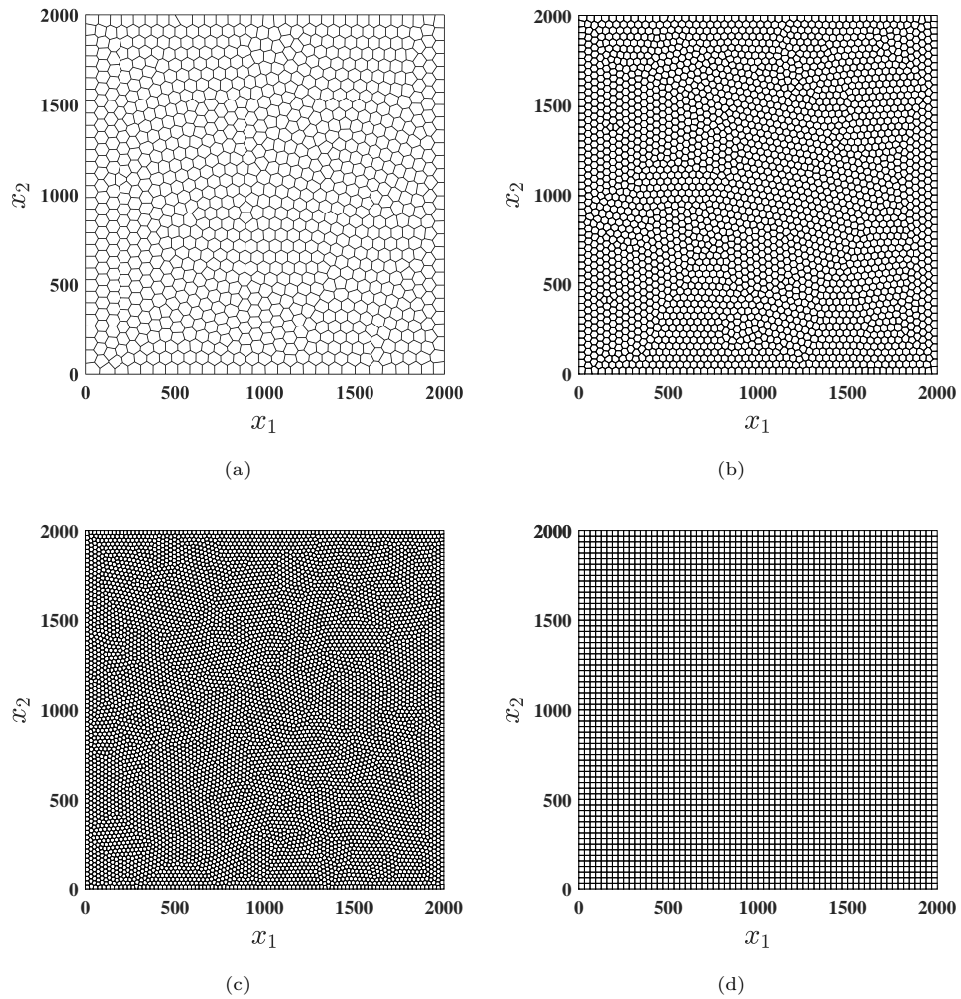


**Fig. 19:** Meshes for the Prandtl's punch test. (a) 4004 DOF polygonal mesh, (b) 12004 DOF polygonal mesh, (c) 32004 DOF polygonal mesh, and (d) 33282 DOF 9-node quadrilateral mesh. Meshes (a)-(c) are used for the VEM and NVEM approaches, whereas mesh (d) is used for the FEM Q9 B-bar approach

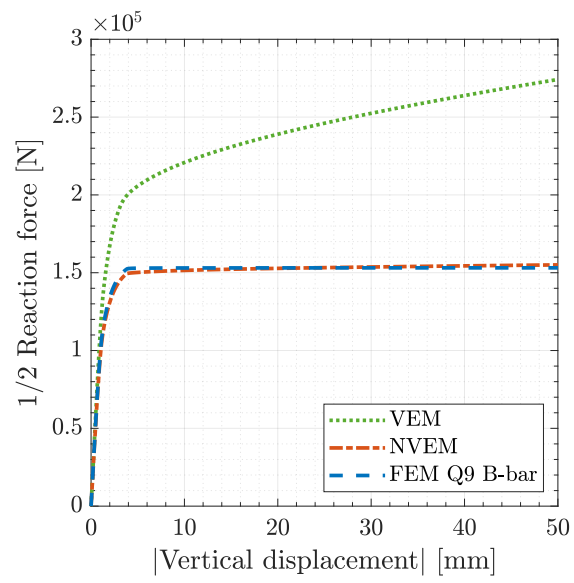


**Fig. 20:** Load-displacement curve for the Prandtl's punch test

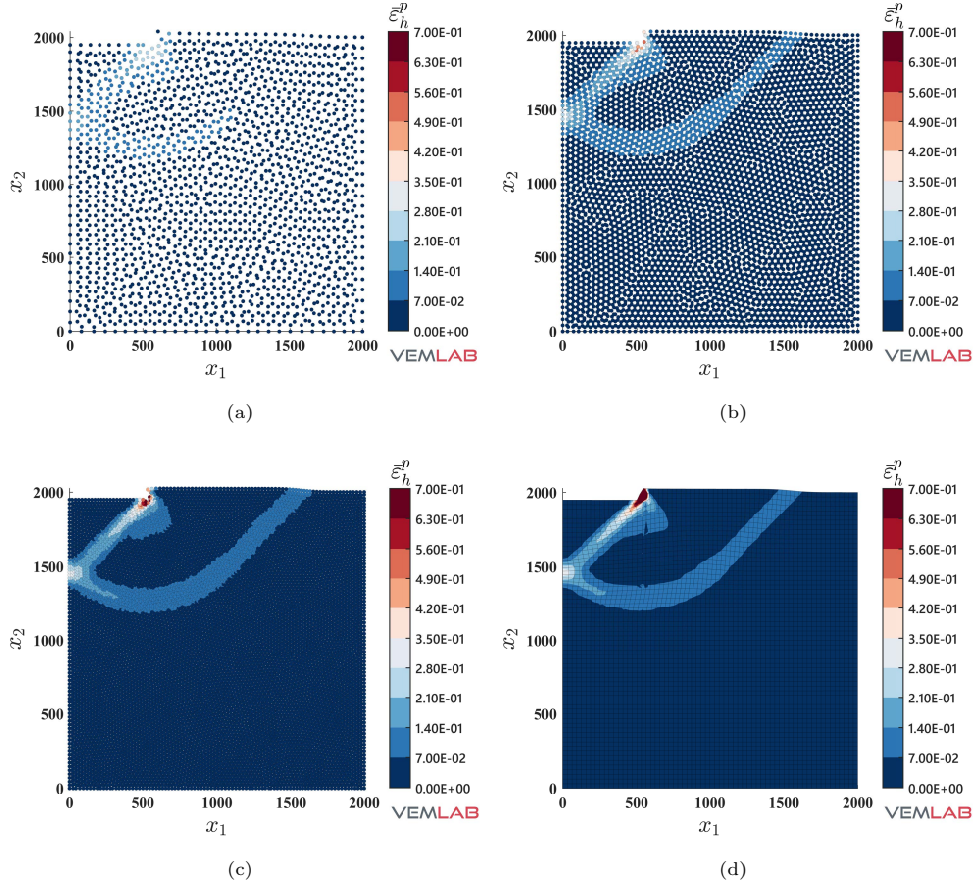


**Fig. 21:** Accumulated plastic strain field solution for the Prandtl's punch test. (a) NVEM (4004 DOF polygonal mesh), (b) NVEM (12004 DOF polygonal mesh), (c) NVEM (32004 DOF polygonal mesh), and (d) FEM Q9 B-bar (33282 DOF 9-node quadrilateral mesh)

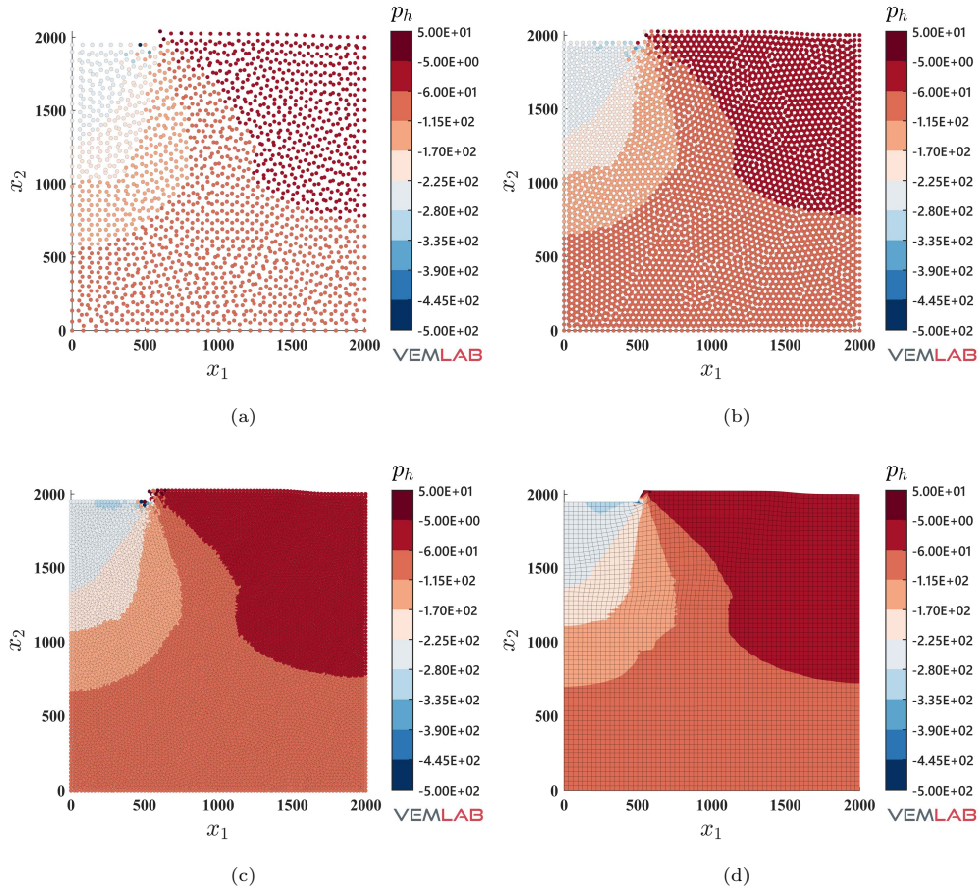


**Fig. 22:** Pressure field solution in MPa for the Prandtl's punch test. (a) NVEM (4004 DOF polygonal mesh), (b) NVEM (12004 DOF polygonal mesh), (c) NVEM (32004 DOF polygonal mesh), and (d) FEM Q9 B-bar (33282 DOF 9-node quadrilateral mesh)

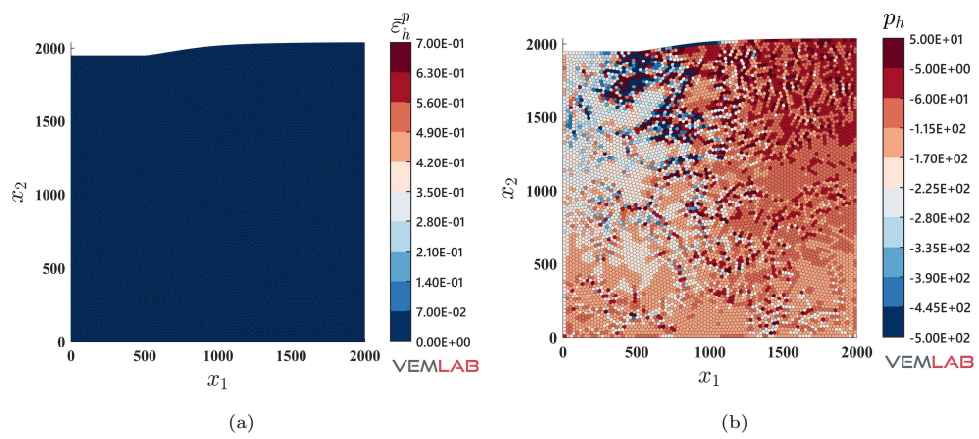


**Fig. 23:** Prandtl's punch test. VEM solution (32004 DOF polygonal mesh) for the (a) accumulated plastic strain, and (b) pressure field in MPa

## References

- [1] Malkus, D.S., Hughes, T.J.R.: Mixed finite element methods – reduced and selective integration techniques: a unification of concepts. *Computer Methods in Applied Mechanics and Engineering* **15**(1), 63–81 (1978)
- [2] Hughes, T.J.R.: Generalization of selective integration procedures to anisotropic and non-linear media. *International Journal for Numerical Methods in Engineering* **15**(9), 1413–1418 (1980)
- [3] Simo, J.C., Hughes, T.J.R.: *Computational Inelasticity*. Springer, USA (1998)
- [4] Simo, J.C., Rifai, S.: A class of mixed assumed strain methods and the method of incompatible modes. *International Journal for Numerical Methods in Engineering* **29**(8), 1595–1638 (1990)
- [5] Bonet, J., Burton, A.J.: A simple average nodal pressure tetrahedral element for incompressible and nearly incompressible dynamic explicit applications. *Communications in Numerical Methods in Engineering* **14**(5), 437–449 (1998)
- [6] Dohrmann, C.R., Heinstein, M.W., Jung, J., Key, S.W., Witkowski, W.R.: Node-based uniform strain elements for three-node triangular and four-node tetrahedral meshes. *International Journal for Numerical Methods in Engineering* **47**(9), 1549–1568 (2000)
- [7] Bonet, J., Marriott, H., Hassan, O.: An averaged nodal deformation gradient linear tetrahedral element for large strain explicit dynamic applications. *Communications in Numerical Methods in Engineering* **17**(8), 551–561 (2001)
- [8] Puso, M.A., Solberg, J.: A stabilized nodally integrated tetrahedral. *International Journal for Numerical Methods in Engineering* **67**(6), 841–867 (2006)
- [9] Puso, M.A., Chen, J.-S., Zywicz, E., Elmer, W.: Meshfree and finite element nodal integration methods. *International Journal for Numerical Methods in Engineering* **74**(3), 416–446 (2008)
- [10] Krysl, P., Zhu, B.: Locking-free continuum displacement finite elements with nodal integration. *International Journal for Numerical Methods in Engineering* **76**(7), 1020–1043 (2008)
- [11] Brocardo, M., Micheloni, M., Krysl, P.: Assumed-deformation gradient finite elements with nodal integration for nearly incompressible large deformation analysis. *International Journal for Numerical Methods in Engineering* **78**(9), 1113–1134 (2009)
- [12] Castellazzi, G., Krysl, P.: Patch-averaged assumed strain finite elements for stress analysis. *International Journal for Numerical Methods in Engineering* **90**(13),

1618–1635 (2012)

- [13] Krysl, P., Kagey, H.: Reformulation of nodally integrated continuum elements to attain insensitivity to distortion. *International Journal for Numerical Methods in Engineering* **90**(7), 805–818 (2012)
- [14] Artioli, E., Castellazzi, G., Krysl, P.: Assumed strain nodally integrated hexahedral finite element formulation for elastoplastic applications. *International Journal for Numerical Methods in Engineering* **99**(11), 844–866 (2014)
- [15] Beirão da Veiga, L., Brezzi, F., Cangiani, A., Manzini, G., Marini, L.D., Russo, A.: Basic principles of virtual element methods. *Mathematical Models and Methods in Applied Sciences* **23**(1), 199–214 (2013)
- [16] Cangiani, A., Manzini, G., Russo, A., Sukumar, N.: Hourglass stabilization and the virtual element method. *International Journal for Numerical Methods in Engineering* **102**(3–4), 404–436 (2015)
- [17] Beirão da Veiga, L., Brezzi, F., Marini, L.D.: Virtual elements for linear elasticity problems. *SIAM Journal on Numerical Analysis* **51**(2), 794–812 (2013)
- [18] Beirão da Veiga, L., Lovadina, C., Mora, D.: A Virtual Element Method for elastic and inelastic problems on polytope meshes. *Computer Methods in Applied Mechanics and Engineering* **295**, 327–346 (2015)
- [19] Artioli, E., Beirão da Veiga, L., Lovadina, C., Sacco, E.: Arbitrary order 2D virtual elements for polygonal meshes: part I, elastic problem. *Computational Mechanics* **60**(3), 355–377 (2017)
- [20] Artioli, E., Beirão da Veiga, L., Lovadina, C., Sacco, E.: Arbitrary order 2D virtual elements for polygonal meshes: part II, inelastic problem. *Computational Mechanics* **60**(4), 643–657 (2017)
- [21] Park, K., Chi, H., Paulino, G.H.: B-bar virtual element method for nearly incompressible and compressible materials. *Meccanica* **56**(6), 1423–1439 (2021)
- [22] Gain, A.L., Talischi, C., Paulino, G.H.: On the virtual element method for three-dimensional linear elasticity problems on arbitrary polyhedral meshes. *Computer Methods in Applied Mechanics and Engineering* **282**, 132–160 (2014)
- [23] D’Altri, A.M., de Miranda, S., Patruno, L., Sacco, E.: An enhanced vem formulation for plane elasticity. *Computer Methods in Applied Mechanics and Engineering* **376**, 113663 (2021)
- [24] Tang, X., Liu, Z., Zhang, B., Feng, M.: A low-order locking-free virtual element for linear elasticity problems. *Computers & Mathematics with Applications* **80**(5), 1260–1274 (2020)

- [25] Cihan, M., Hudobivnik, B., Aldakheel, F., Wriggers, P.: 3D mixed virtual element formulation for dynamic elasto-plastic analysis. *Computational Mechanics* **68**(3), 1–18 (2021)
- [26] Park, K., Chi, H., Paulino, G.H.: Numerical recipes for elastodynamic virtual element methods with explicit time integration. *International Journal for Numerical Methods in Engineering* **121**(1), 1–31 (2020)
- [27] Park, K., Chi, H., Paulino, G.H.: On nonconvex meshes for elastodynamics using virtual element methods with explicit time integration. *Computer Methods in Applied Mechanics and Engineering* **356**, 669–684 (2019)
- [28] Wriggers, P., Rust, W.T.: A virtual element method for frictional contact including large deformations. *Engineering Computations* **36**(7), 2133–2161 (2019)
- [29] De Bellis, M.L., Wriggers, P., Hudobivnik, B.: Serendipity virtual element formulation for nonlinear elasticity. *Computers & Structures* **223**, 106094 (2019)
- [30] Aldakheel, F., Hudobivnik, B., Wriggers, P.: Virtual elements for finite thermo-plasticity problems. *Computational Mechanics* **64**(5), 1347–1360 (2019)
- [31] Wriggers, P., Hudobivnik, B.: A low order virtual element formulation for finite elasto-plastic deformations. *Computer Methods in Applied Mechanics and Engineering* **327**, 459–477 (2017)
- [32] Wriggers, P., Reddy, B.D., Rust, W., Hudobivnik, B.: Efficient virtual element formulations for compressible and incompressible finite deformations. *Computational Mechanics* **60**(2), 253–268 (2017)
- [33] Hudobivnik, B., Aldakheel, F., Wriggers, P.: A low order 3D virtual element formulation for finite elasto-plastic deformations. *Computational Mechanics* **63**(2), 253–269 (2019)
- [34] Zhang, X.S., Chi, H., Paulino, G.H.: Adaptive multi-material topology optimization with hyperelastic materials under large deformations: A virtual element approach. *Computer Methods in Applied Mechanics and Engineering* **370**, 112976 (2020)
- [35] Chi, H., Beirão da Veiga, L., Paulino, G.H.: Some basic formulations of the virtual element method (VEM) for finite deformations. *Computer Methods in Applied Mechanics and Engineering* **318**, 148–192 (2017)
- [36] van Huyssteen, D., Reddy, B.D.: A virtual element method for isotropic hyperelasticity. *Computer Methods in Applied Mechanics and Engineering* **367**, 113134 (2020)
- [37] Wriggers, P., Rust, W.T., Reddy, B.D.: A virtual element method for contact.

Computational Mechanics **58**(6), 1039–1050 (2016)

- [38] Aldakheel, F., Hudobivnik, B., Artioli, E., Beirão da Veiga, L., Wriggers, P.: Curvilinear virtual elements for contact mechanics. *Computer Methods in Applied Mechanics and Engineering* **372**, 113394 (2020)
- [39] Aldakheel, F., Hudobivnik, B., Wriggers, P.: Virtual element formulation for phase-field modeling of ductile fracture. *International Journal for Multiscale Computational Engineering* **17**(2), 181–200 (2019)
- [40] Hussein, A., Aldakheel, F., Hudobivnik, B., Wriggers, P., Guidault, P.-A., Allix, O.: A computational framework for brittle crack-propagation based on efficient virtual element method. *Finite Elements in Analysis and Design* **159**, 15–32 (2019)
- [41] Nguyen-Thanh, V.M., Zhuang, X., Nguyen-Xuan, H., Rabczuk, T., Wriggers, P.: A Virtual Element Method for 2d linear elastic fracture analysis. *Computer Methods in Applied Mechanics and Engineering* **340**, 366–395 (2018)
- [42] Benedetto, M.F., Caggiano, A., Etse, G.: Virtual elements and zero thickness interface-based approach for fracture analysis of heterogeneous materials. *Computer Methods in Applied Mechanics and Engineering* **338**, 41–67 (2018)
- [43] Artioli, E., Marfia, S., Sacco, E.: VEM-based tracking algorithm for cohesive/frictional 2d fracture. *Computer Methods in Applied Mechanics and Engineering* **365**, 112956 (2020)
- [44] Beirão da Veiga, L., Pichler, A., Vacca, G.: A virtual element method for the miscible displacement of incompressible fluids in porous media. *Computer Methods in Applied Mechanics and Engineering* **375**, 113649 (2021)
- [45] Chen, L., Wang, F.: A Divergence Free Weak Virtual Element Method for the Stokes Problem on Polytopal Meshes. *Journal of Scientific Computing* **78**(2), 864–886 (2019)
- [46] Gatica, G.N., Munar, M., Sequeira, F.A.: A mixed virtual element method for the Navier–Stokes equations. *Mathematical Models and Methods in Applied Sciences* **28**(14), 2719–2762 (2018)
- [47] Beirão da Veiga, L., Lovadina, C., Vacca, G.: Virtual elements for the Navier–Stokes problem on polygonal meshes. *SIAM Journal on Numerical Analysis* **56**(3), 1210–1242 (2018)
- [48] Chernov, A., Marcati, C., Mascotto, L.: p- and hp- virtual elements for the Stokes problem. *Advances in Computational Mathematics* **47**(2), 24 (2021)

- [49] Andersen, O., Nilsen, H.M., Raynaud, X.: Virtual element method for geomechanical simulations of reservoir models. *Computational Geosciences* **21**(5), 877–893 (2017)
- [50] Lin, S., Zheng, H., Jiang, W., Li, W., Sun, G.: Investigation of the excavation of stony soil slopes using the virtual element method. *Engineering Analysis with Boundary Elements* **121**, 76–90 (2020)
- [51] Gain, A.L., Paulino, G.H.: Bridging art and engineering using Escher-based virtual elements. *Structural and Multidisciplinary Optimization* **51**, 867–883 (2015)
- [52] Chi, H., Pereira, A., Menezes, I.F.M., Paulino, G.H.: Virtual element method (VEM)-based topology optimization: an integrated framework. *Structural and Multidisciplinary Optimization* **62**(3), 1089–1114 (2020)
- [53] Artioli, E., Miranda, S., Lovadina, C., Patruno, L.: A stress/displacement virtual element method for plane elasticity problems. *Computer Methods in Applied Mechanics and Engineering* **325**, 155–174 (2017)
- [54] Dassi, F., Lovadina, C., Visinoni, M.: Hybridization of the virtual element method for linear elasticity problems. *Mathematical Models and Methods in Applied Sciences* **31**(14), 2979–3008 (2021)
- [55] Kwak, D.Y., Park, H.: Lowest-order virtual element methods for linear elasticity problems. *Computer Methods in Applied Mechanics and Engineering* **390**, 114448 (2022)
- [56] Zhang, B., Zhao, J., Yang, Y., Chen, S.: The nonconforming virtual element method for elasticity problems. *Journal of Computational Physics* **378**, 394–410 (2019)
- [57] Yu, Y.: A lowest-order locking-free nonconforming virtual element method based on the reduced integration technique for linear elasticity problems. *Computers & Mathematics with Applications* **135**, 157–170 (2023)
- [58] Xu, B.-B., Wang, Y.-F., Wriggers, P.: Stabilization-free virtual element method for 2D elastoplastic problems. *International Journal for Numerical Methods in Engineering* **125**(15), 22 (2024)
- [59] Liguori, F.S., Madeo, A., Marfia, S., Garcea, G., Sacco, E.: A stabilization-free hybrid virtual element formulation for the accurate analysis of 2D elasto-plastic problems. *Computer Methods in Applied Mechanics and Engineering* **431**, 117281 (2024)
- [60] Ortiz-Bernardin, A., Silva-Valenzuela, R., Salinas-Fernández, S., Hitschfeld-Kahler, N., Luza, S., Rebolledo, B.: A node-based uniform strain virtual element

- method for compressible and nearly incompressible elasticity. *International Journal for Numerical Methods in Engineering* **124**(8), 1818–1855 (2023)
- [61] Beirão da Veiga, L., Brezzi, F., Marini, L.D., Russo, A.: The hitchhiker’s guide to the virtual element method. *Mathematical Models and Methods in Applied Sciences* **24**(08), 1541–1573 (2014)
- [62] Ortiz-Bernardin, A., Russo, A., Sukumar, N.: Consistent and stable meshfree Galerkin methods using the virtual element decomposition. *International Journal for Numerical Methods in Engineering* **112**(7), 655–684 (2017)
- [63] Ortiz-Bernardin, A., Alvarez, C., Hitschfeld-Kahler, N., Russo, A., Silva-Valenzuela, R., Olate-Sanzana, E.: Veamy: an extensible object-oriented C++ library for the virtual element method. *Numerical Algorithms* **82**(4), 1189–1220 (2019)
- [64] Silva-Valenzuela, R., Ortiz-Bernardin, A., Sukumar, N., Artioli, E., Hitschfeld-Kahler, N.: A nodal integration scheme for meshfree galerkin methods using the virtual element decomposition. *International Journal for Numerical Methods in Engineering* **121**(10), 2174–2205 (2020)
- [65] Hughes, T.J.R.: *The Finite Element Method: Linear Static and Dynamic Finite Element Analysis*. Dover Publications, Inc, Mineola, NY (2000)
- [66] Beirão da Veiga, L., Dassi, F., Russo, A.: High-order virtual element method on polyhedral meshes. *Computers & Mathematics with Applications* **74**(5), 1110–1122 (2017)
- [67] Mascotto, L.: Ill-conditioning in the virtual element method: Stabilizations and bases. *Numerical Methods for Partial Differential Equations* **34**(4), 1258–1281 (2018)
- [68] Souza Neto, E.A., Perić, D., Owen, D.R.J.: *Computational Methods for Plasticity: Theory and Applications*. John Wiley & Sons Ltd, UK (2008)
- [69] Tan, T.-M., Li, S., Chou, P.C.: Finite element solution of Prandtl’s flat punch problem. *Finite Elements in Analysis and Design* **6**(2), 173–186 (1989)